

# Challenges in $\text{Sr}_2\text{FeMoO}_{6-\delta}$ Thin Film Deposition

Gunnar Suchaneck,\* Nikolay Kalanda, Evgenij Artsiukh, and Gerald Gerlach

This work reviews some fundamental issues that are relevant for the fabrication of stable-phase strontium ferromolybdate thin films. The main challenges for strontium ferromolybdate thin film deposition arise from the sensitivity of the material's magnetic properties to point defect formation: i) Antisite defect formation and oxygen nonstoichiometry should be avoided by precise composition control during film manufacturing; ii) a highly ordered state of the correct phase and B-site cation valence will be obtained only in a very narrow window of growth conditions; iii) to avoid additional antisite disorder with decreasing synthesis temperature, the effective temperature at the film surface should be increased by an energy flux to the growing film surface. Since thin film deposition is non-equilibrium in nature, the review starts with the consideration of equilibrium phase stability. Cation and oxygen stoichiometries are analyzed with regard to their effect on key magnetic properties. Film strain formed due to thermal and lattice mismatch is of great concern since it influences the choice of the substrate. Finally, thin film deposition techniques are valued for their benefits in strontium ferromolybdate thin film technology.

## 1. Introduction

The era of oxide perovskites with ferromagnetic behavior around room temperature was opened in 1950 by pioneering studies on  $\text{La}_{1-x}\text{Ca}_x\text{MnO}_3$  ( $0.2 < x < 0.4$ ).<sup>[1]</sup> The discovery of low-field magnetoresistance (LFMR) and half-metallicity of the strontium ferromolybdate ( $\text{Sr}_2\text{FeMoO}_{6-\delta}$ , SFMO) compound by Kobayashi et al. in 1998<sup>[2]</sup> renewed the interest in these materials in the context of their potential applications in the field of spin electronics. The number of publications in the following years (Figure 1) reproduces a Gartner hype cycle for emerging technologies<sup>[3]</sup>; Kobayashi's article triggered an increasing interest until the peak of inflated

expectations was reached, followed by a trough of disillusionment and afterwards a renewed interest to be seen as a slope of enlightenment. What should be expected now is the plateau of productivity. However, this phase has not yet occurred. The main reasons for the still-missing wide application of SFMO is the low reproducibility of its magnetic properties originating in cation and oxygen stoichiometry issues and its aging in contact with air and moisture. On the other hand, research focusing on thin films most promising for device fabrication is still a small fraction of the SFMO publication activities (cf. Figure 1).

The physical origin of magnetoresistance in SFMO is the half-metallic nature of the ground state, that is, the material is a semiconductor for the up-spin band, but a metal for the down-spin band, since the latter is continuous at the Fermi level. This theoretically leads to a complete spin polarization at the Fermi level, making

SFMO suitable for applications as a source of spin-polarized charge carriers in spintronic devices.<sup>[2]</sup> The ideal structure of an  $\text{A}_2\text{B}'\text{B}''\text{O}_6$  double-perovskite lattice can be viewed as a 3D checkerboard of alternating  $\text{B}'\text{O}_6$  and  $\text{B}''\text{O}_6$  octahedra. The A cations reside in the cuboctahedral cavities created by the corner-sharing octahedral (Figure 2a).

Maintaining the half-metallic ferrimagnetic character of SFMO is one of the key issues for its industrial applications in magnetoresistive and spintronic devices. First-principle calculations reveal that the most abundant point defects in SFMO are oxygen vacancies (Figure 2b) as well as antisite defect pairs  $\text{Fe}_{\text{Mo}}$  and  $\text{Mo}_{\text{Fe}}$  (Figure 2c).<sup>[6]</sup> They yield a diminution of half-metallic character by  $\text{Fe}_{\text{Mo}}$  antisite defects and Mo vacancies, that is, in Fe-rich SFMO films,<sup>[6,7]</sup> as well as by  $\text{Fe}_{\text{Mo}} + \text{Mo}_{\text{Fe}}$  pairs.<sup>[5–13]</sup> According to other first-principle calculations, the half-metallic characters are maintained for SFMO containing  $\text{Fe}_{\text{Mo}}$  and Fe vacancies (i.e., in Mo-rich films),<sup>[7]</sup> oxygen vacancies,<sup>[7,11,13–15]</sup> or Sr vacancies.<sup>[7]</sup> This illustrates that SFMO is a material that is very sensitive to Fe-excess, but less sensitive to oxygen- and Sr-deficit.

The understanding of the degree of deviation from equilibrium during film growth as well as the point defect formation mechanisms is fundamental for the optimization of physical properties with regard to device application. Defects deteriorating half-metallicity should be avoided.<sup>[7]</sup> Additionally, it was suggested to increase the amount of oxygen vacancies so as to improve  $T_C$  since they do not even deteriorate spin polarization, a key parameter for applications.<sup>[13]</sup> A larger  $M_s$  was predicted in the presence of small amounts of strontium vacancies since a deficit of strontium without the formation of oxygen vacancies

Dr. G. Suchaneck, Prof. G. Gerlach  
Solid State Electronics Laboratory  
TU Dresden  
Dresden 01062, Germany  
E-mail: Gunnar.Suchaneck@tu-dresden.de

Dr. N. Kalanda, E. Artsiukh  
SSPA Scientific and Practical Materials Research Center of NAS of Belarus  
Division of Cryogenic Research  
Minsk 220072, Belarus

 The ORCID identification number(s) for the author(s) of this article can be found under <https://doi.org/10.1002/pssb.201900312>.

© 2019 The Authors. Published by WILEY-VCH Verlag GmbH & Co. KGaA, Weinheim. This is an open access article under the terms of the Creative Commons Attribution License, which permits use, distribution and reproduction in any medium, provided the original work is properly cited.

DOI: 10.1002/pssb.201900312

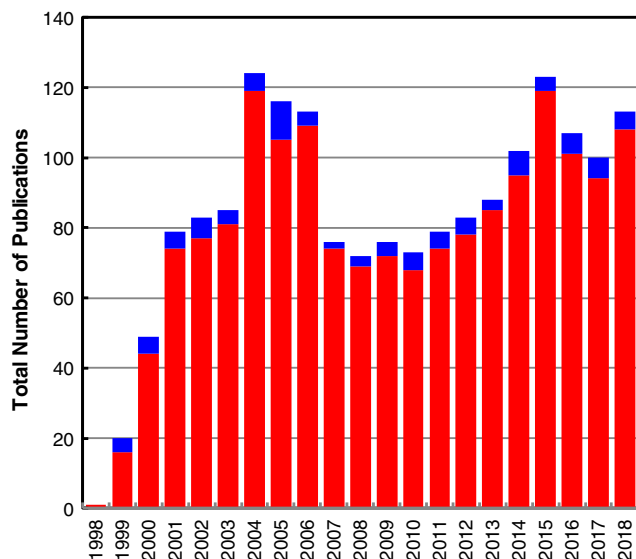


**Figure 1.** Number of SFMO publications recorded by the Web of Science for each year. The blue part indicates the fraction of publications on SFMO thin films.

will increase the valence of Fe and Mo to ensure electrical neutrality of the formula unit.<sup>[12]</sup> The same holds for molybdenum vacancies ( $V_{Mo}$ ) where most of the injected holes are mainly localized at Mo sites.<sup>[16]</sup>

In stoichiometric SFMO, the order parameter  $S$  is related to the fraction of ions  $B'$  (or  $B''$ ) on the wrong sublattice called antisite disorder (ASD)<sup>[17]</sup>:

$$S = (1 - 2ASD) \quad (1)$$

Here, the value of ASD varies from 0 (corresponding to a complete order) up to 0.5, describing a completely random Fe-Mo site occupancy.

Magnetic tunnel junctions (MTJs) use materials with almost ideal (100%) spin polarization. These devices consist of two ferromagnetic layers sandwiching a very thin barrier layer of an insulator material.<sup>[18]</sup> The resistance of MTJs is highest when the magnetic moments in two ferromagnetic layers are anti-aligned, and lowest when they are aligned. The ratio between these values is called magnetoresistance ratio (MR). A first pico-tesla magnetic field sensor using spin-dependent tunneling devices was presented in 1998.<sup>[19]</sup> MTJs may exhibit extremely high MR values. Theoretically it reaches 1000% in Fe/MgO/Fe structures.<sup>[20,21]</sup>  $Sr_2FeMoO_6/SrTiO_3/Sr_2FeMoO_6$  trilayer MTJ devices show a tunneling MR of  $\approx 7\%$  at room temperature.<sup>[22]</sup>

Nowadays, SFMO is the most studied ferrimagnetic double perovskite. SFMO double perovskites are promising candidates for magnetic electrode materials for room-temperature spintronics applications, because they present a half-metallic character (with theoretically 100% polarization), a high Curie temperature ( $T_C$ ) of about 415 K (ferromagnets should be operated in their ordered magnetic state below  $T_C$ ), and a low-field magnetoresistance.<sup>[2]</sup>

As there is still no clarity about the effect of point defects on SFMO magnetic properties, in the following we will consider the role of phase stability and point defects in SFMO (Section 2) and



**Gunnar Suchaneck** is currently Senior Researcher and Chief Assistant of the Solid State Electronics Laboratory at TU Dresden, Germany. He received his Ph.D. in physico-mathematical sciences from the Electrotechnical University–LETI, St. Petersburg, Russia, in 1983. His current research interests include solid-state sensor technology: ferroelectric thin-film materials, metal oxide thin films, thin film deposition by reactive sputtering and plasma-enhanced chemical vapor deposition, and characterization of thin films by optical and electrical measurements. He has co-authored more than 280 technical publications in books, scientific journals, and conference proceedings, and has co-authored 15 patents.



**Nikolay Kalanda** received his Ph.D. degree from the National Academy of Sciences of Belarus in 2002. His research activities deal with the synthesis and investigations of charge transfer mechanisms in bulk, thin-film, and powder samples on the base of complex metal oxides having the double perovskite structure. In the last years, he has supported research collaboration with colleagues in Russia, Germany, France, Lithuania, Portugal, and South Korea; he has taken an active part in various international research projects (DAAD, DFG, ERASMUS-MUNDUS, IRSES, MSCA-RISE). He is author and co-author of more than 250 papers.



**Evgenij Artiukh** is currently Junior Research Fellow and PhD student of the SSPA “Scientific-Practical Materials Research Centre of NAS of Belarus,” Minsk, Belarus. He received his master’s degree from Belarusian State University of Informatics and Radioelectronics (BSUIR) Minsk, Belarus, in 2017. His current research interests include solid-state physics and micro- and nanoelectronic technology: spintronics, magnetics, metal oxide thin film deposition by reactive sputtering and plasma-enhanced chemical vapor deposition.

the impact of the latter on its magnetic properties (Section 3). Section 4 is devoted to particular problems of SFMO thin film deposition. Finally, this feature article is completed by conclusions.

## 2. Phase Stability and Point Defects in $Sr_2FeMoO_{6-\delta}$

### 2.1. Equilibrium Phase Stability

Phase diagrams of the system  $SrO-Fe_3O_4-MoO_3$  at 1200 °C are available in air<sup>[23]</sup> and in Ar with 1%  $H_2$ .<sup>[24]</sup> In air, the

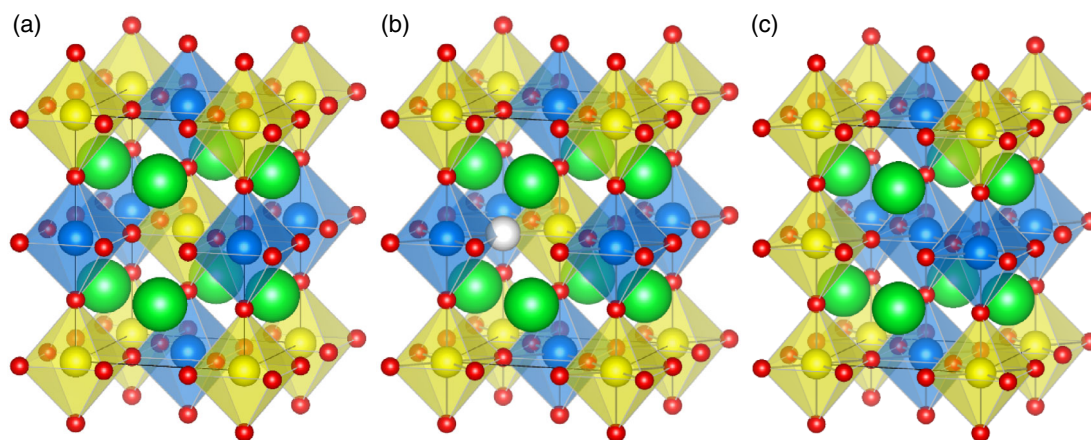


**Figure 2.** a) Ideal lattice structure of SFMO, b) SFMO lattice consisting of an oxygen vacancy, and c) an antisite defect pair. The atoms are shown as colored balls (Sr, green; Fe, blue; Mo, yellow; O, red). These images were drawn using the 3D visualization program for structural models, VESTA.<sup>[4]</sup>

solubility of  $\text{SrMoO}_4$  in  $\text{SrFeO}_{3-\delta}$  is about 17 mol% (up to  $\text{Sr}_2\text{Fe}_{1.34}\text{Mo}_{0.68}\text{O}_{6-\delta}$ ), that of  $\text{SrFeO}_{3-\delta}$  in  $\text{SrMoO}_4$  amounts to 2.2 mol%. Consequently,  $\text{Sr}_2\text{FeMoO}_{6-\delta}$  in air is thermodynamically unstable due to insufficient Mo and Fe solubilities in  $\text{SrFeO}_{3-\delta}$  and  $\text{SrMoO}_4$ , respectively. In fact, a sample of  $\text{Sr}_2\text{FeMoO}_{6-\delta}$  annealed at 1200 °C in Ar was found to contain 10% of a second phase of  $\text{SrMoO}_4$ .<sup>[25]</sup> In 1%  $\text{H}_2/\text{Ar}$ , the solubility of Mo in  $\text{SrFeO}_{3-\delta}$  extends to 29 mol%, that is, the homogeneity region of the solid solution of  $\text{SrFeO}_{3-\delta}$  exceeds that of  $\text{Sr}_2\text{Fe}_{0.92}\text{Mo}_{1.08}\text{O}_{6-\delta}$ . Here, oxygen nonstoichiometry  $\delta$  was found to approach a value of 0.2, reducing also the cation valence.<sup>[24]</sup> Contrarily, other authors obtained a maximum oxygen nonstoichiometry of 0.086 under similar conditions at 1200 °C in 2%  $\text{H}_2/\text{Ar}$ .<sup>[26,27]</sup>

Stoichiometric  $\text{Sr}_2\text{FeMoO}_{6-\delta}$  (SFMO) is thermodynamically stable at 1200 °C only in a narrow window of oxygen partial pressures of  $3.20 \times 10^{-9} \leq p_{\text{O}_2} \leq 1.61 \times 10^{-5}$  Pa.<sup>[28]</sup> By reduction it decomposes into  $\text{SrO} + \text{Mo} + \varepsilon\text{-Fe}_3\text{Mo}_2$  and by oxidation into  $\text{SrMoO}_4 + \text{SrFeO}_{3-\delta}$ . According to ref. [26,27], the phase stability of SFMO at 1200 °C ranges from  $p_{\text{O}_2} = 2.0 \times 10^{-9}$  to  $6.39 \times 10^{-6}$  Pa. Increasing oxygen partial pressure, oxygen nonstoichiometry will be reduced up to the point where  $\delta \approx 0$ . Above this point, excess oxygen is accommodated by  $\text{SrMoO}_4$  phase formation. Following ref. [29], SFMO is thermodynamically stable below oxygen partial pressures of  $1.0 \times 10^{-6}$ – $2.8 \times 10^{-6}$  Pa in the temperature range of 1140–1220 °C with an oxygen partial molar enthalpy of  $1.73 \pm 0.08$  eV. Thus, with regard to the cation-to-anion ratio, SFMO possesses a one-sided homogeneity region (Figure 3).

At 1200 °C, SFMO can be completely synthesized in an atmosphere of 5%  $\text{H}_2$  in  $\text{N}_2$ .<sup>[30]</sup> It decomposes in air to form  $\text{SrMoO}_4$  and  $\text{Sr}_2\text{Fe}_{2-x}\text{Mo}_x\text{O}_6$  rather than  $\text{SrFeO}_3$  following the reduction of the solubility of molybdenum ions in SFMO. The synthesis of SFMO in a reducing atmosphere is attributed to the creation of oxygen vacancies. When Mo ions substitute Fe ions, the radii of  $\text{Fe}^{3+}$  and  $\text{Mo}^{5+}$  in SFMO become larger than the one of  $\text{Fe}^{4+}$  in  $\text{SrFeO}_3$ . The required larger unit cell volume is then provided by oxygen vacancies. In a reducing 1%  $\text{H}_2/\text{Ar}$  atmosphere, the solubility of  $\text{SrMoO}_4$  in  $\text{SrFeO}_{3-\delta}$  is about 30%, that is, beyond

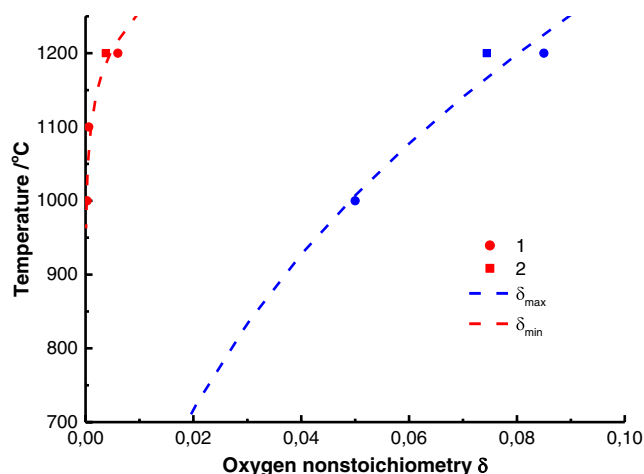


**Figure 3.** SFMO homogeneity region based on data in refs. [27] (1), [28] (2) and represented in dependence on the lower and upper limits of the oxygen nonstoichiometry parameter  $\delta$  (cf. Equation (7)) at equilibrium.

the point of SFMO formation. In air, SFMO will be unstable since here the solubility of  $\text{SrMoO}_4$  does not exceed 16.5% needed to form a mixture  $\text{SrFe}_{1-x}\text{Mo}_x\text{O}_{6-\delta}$  and  $\text{SrMoO}_4$  at higher Mo content.<sup>[24]</sup> Above the minimum oxygen deficiency  $\delta_{\text{min}}$ , SFMO oxidizes according to



Below  $\delta_{\text{max}}$  it is reduced, resulting in  $\text{Sr}_3\text{FeMoO}_7$  and  $\text{Fe}$ .<sup>[27]</sup> For instance, a nonmagnetic minority phase of 10%  $\text{SrMoO}_4$  was obtained in SFMO sintered for 2 h in pure Ar at 1200 °C.<sup>[25]</sup> As a result, achieving a precise stoichiometric ratio of Sr:Fe:Mo = 2:1:1 in a sample is not trivial.

It has to be noted that the above-stated  $p_{\text{O}_2}$  values are below the ones in an atmosphere of ultra-high purity Ar 5.0 ( $\geq 99.999$  vol% Ar). On the other hand, thin film deposition is a thermodynamically nonequilibrium process, that is, phase formation during film growth and evolution of the film texture are determined

by kinetics of adsorption, diffusion, and other processes. Consequently, the material properties not only are very sensitive to synthesis and processing conditions, such as temperature and rate of temperature changes, composition of gas atmosphere, phase formation rate, as well as atmosphere for postsynthesis heat treatment, but also will deteriorate with time, since the film is in a metastable state. Evidence of SFMO metastability at room temperature is given by a sudden increase of resistivity of polycrystalline samples after exposing them to air.<sup>[31]</sup> This was attributed to a change of oxygen content at grain boundaries. SFMO thin films grown by pulsed laser deposition (PLD) in vacuum age significantly with time, while those grown in Ar atmosphere are comparably much more stable.<sup>[32]</sup> The transition of a 40-nm-thick SFMO thin film into its aged state within 8 days yields a room temperature diffusion coefficient of  $\approx 2 \times 10^{-17} \text{ cm}^2 \text{ s}^{-1}$ , which is in good agreement with the extrapolation of oxygen vacancy diffusion data in perovskites<sup>[33]</sup> down to lower temperatures. Air exposure of sputter-deposited SFMO films at room temperature indicates the formation of a SrMoO<sub>4</sub> surface barrier layer with a thickness of about 0.9 nm per month.<sup>[34]</sup> Phase decomposition of SFMO with a typical grain size of about 1 μm in air into SrMoO<sub>4</sub> and Fe at room temperature was studied in ref. [35]. In sintered pellets, unit cell expansion and decomposition to SrMoO<sub>4</sub> is rather moderate at room temperature. The fraction of SrMoO<sub>4</sub> increases logarithmically with time. Thereby, there is no noticeable increase of ASD within 48 days. At a higher temperature of 60 °C, SrMoO<sub>4</sub> formation is accelerated. Aging is much stronger in granular thick films prepared by screen printing. Here, phase decomposition is strongly pronounced >300 °C. SFMO transformation is supposed to be triggered by the presence of H<sub>2</sub>O and leads up to total decomposition. The hypothesized reaction products are SrMoO<sub>4</sub>, FeO, and Sr(OH)<sub>2</sub>, which in air are easily transformed with CO<sub>2</sub> into SrCO<sub>3</sub>.<sup>[30]</sup> In a flowing air or nitrogen atmosphere ( $p_{\text{O}_2} \approx 1\text{--}10 \text{ Pa}$ ), Raman scattering, thermogravimetric analysis, and thermomagnetization reveal above 400 °C an irreversible SFMO decomposition into SrMoO<sub>4</sub> and SrFeO<sub>3-δ</sub>.<sup>[36]</sup> This decomposition might be attributed also to a solubility of Mo in SrFeO<sub>3-δ</sub> decreasing with temperature. In fact, Mo evaporation was obtained when SFMO was heated in air.<sup>[30]</sup> The long-term structural decomposition of SFMO in air is accompanied by a gradual shift of the Fe<sup>2+</sup>/Fe<sup>3+</sup> mixed valence state toward Fe<sup>3+</sup>.<sup>[37]</sup> The fraction of Fe<sup>3+</sup> ions in SFMO was found to increase at room temperature from 35% to 40% within 3 years.

## 2.2. Strontium Nonstoichiometry

In SFMO with strontium-deficit, each strontium donates two holes to the electronic system, increasing the valence of the Fe-Mo couple, thus favoring B'/B'' site ordering.<sup>[38]</sup> On the other hand, the higher ASD in strontium-deficit samples compared to stoichiometric ones is explained by the fact that strontium vacancies favor preferential occupation of surrounding B'/B'' sites by Mo<sup>5+</sup>, that is, the cation having a higher formal valence.<sup>[12]</sup> Without the formation of a new oxygen vacancy (V<sub>O</sub>), the valence increase is fully borne by the Mo ions. Therefore, the deterioration of  $M_s$  with increasing ASD will not change much compared to stoichiometric films (cf. Section 3). Note that at a high oxygen

partial pressure (>100 Pa at 1050 °C), strontium vacancies are predicted to become the most abundant point defects in SFMO.<sup>[5]</sup> However, such large oxygen partial pressures are not typical for film deposition conditions.

SFMO compositions with a small excess of strontium contain SrMoO<sub>4-δ</sub> as the main impurity phase.<sup>[12]</sup> The amount of SrMoO<sub>4</sub> in the samples increases with an increase of strontium excess. Assuming that SrMoO<sub>4</sub> results totally from the excess strontium in the sample, the host phase should form with a chemical composition Sr<sub>2</sub>FeMo<sub>1-x</sub>O<sub>6-δ</sub> where  $x$  is the concentration of strontium taken in excess during sample preparation. Evidence for this assumption is given by the experimentally obtained diminution of both lattice constants, which is similar with that observed in Sr<sub>2</sub>FeMo<sub>1-x</sub>O<sub>6-δ</sub>.<sup>[16]</sup> Here, holes donated by V<sub>Mo</sub> formation localize mainly at Mo sites and cause a stronger electrostatic attraction with the intervening oxygen ion. The improved ordering between Fe and Mo cations enhances MR compared to the stoichiometric sample. Experimentally, the decomposition of nominally A-site-deficient Sr<sub>2-γ</sub>FeMoO<sub>6-δ</sub> compositions ( $0 \leq \gamma \leq 0.5$ ) into non-A-site-deficient and Mo-rich Sr<sub>2</sub>Fe<sub>1-γ</sub>Mo<sub>1+γ</sub>O<sub>6-δ</sub> double perovskites was obtained under synthesis conditions (reducing H<sub>2</sub>/Ar atmosphere at 1350–1400 °C) in ref. [39]. It is accompanied by a gradual transition from the largely B-site-ordered composition at  $\gamma = 0$  to the fully disordered one at  $\gamma = 0.2$ . The behavior of Sr<sub>2</sub>Fe<sub>1-γ</sub>Mo<sub>1+γ</sub>O<sub>6-δ</sub> compounds is additionally discussed in Section 2.3.

When the amount of additional Sr is increased to a ratio allowing the formation of an extra rocksalt-structured SrO layer, Ruddlesden–Popper phases will occur.<sup>[40]</sup> These excess SrO layers are a common defect in perovskite materials such as SrTiO<sub>3</sub>,<sup>[41]</sup> SrCeO<sub>3</sub>,<sup>[42]</sup> Sr<sub>3</sub>Fe<sub>2</sub>O<sub>6-δ</sub>,<sup>[30]</sup> Sr<sub>2</sub>Mn<sub>0.5</sub>Ru<sub>0.5</sub>O<sub>4</sub> and Sr<sub>3</sub>MnRuO<sub>7</sub>,<sup>[43]</sup> Sr<sub>3</sub>Fe<sub>2-x</sub>Mn<sub>x</sub>O<sub>7-δ</sub>,<sup>[44]</sup> Sr<sub>3</sub>Fe<sub>2-x</sub>Co<sub>x</sub>O<sub>7-δ</sub>,<sup>[45]</sup> and others. In Sr<sub>3</sub>FeMoO<sub>7-δ</sub>, every two layers of transition metal BO<sub>6</sub> (B = Fe, Mo) octahedral planes are interrupted along the  $c$ -direction by one SrO layer. The extra SrO layer in Ruddlesden–Popper phase intergrowths of SFMO thin films with a slight Sr-excess disrupts the strong Mo-Fe FM coupling, leading to a deterioration of  $M_s$ .<sup>[46]</sup> Also, the intercalation of conducting perovskite ABO<sub>3</sub> layers by insulating AO layer results in a substantial 2D character of selected physical properties. Two-dimensional BO<sub>6</sub> layers are found to form highly ordered Fe-O-Mo flat nanodomains separated by antiphase boundaries. The interaction between these disc-like ordered domains gives rise to interesting magnetic, transport, and magnetotransport properties.<sup>[47]</sup> A special feature is that Fe and Mo ions are randomly distributed on the B-site at room temperature (similarly to B-site nonstoichiometric SFMO; cf. Section 2.3)<sup>[40,48,49]</sup> with a small fraction of B-site and oxygen vacancies as well as stacking faults along the  $c$ -axis.<sup>[48,49]</sup> Annealing in 5% H<sub>2</sub>/Ar at 900 and 1000 °C, respectively, does not improve B-site ordering.<sup>[49]</sup> The two B-sites are antiferromagnetically coupled. However, there are still controversies about the magnetic properties of Sr<sub>3</sub>FeMoO<sub>7-δ</sub> at low temperatures.<sup>[48,49]</sup> Note that ceramic manufacturing by the solid-state reaction method is not capable of preparing a fully oxygenated Sr<sub>3</sub>FeMoO<sub>7</sub> phase. The oxygen vacancies in the resulting Sr<sub>3</sub>FeMoO<sub>6.88</sub> compound occur preferentially between the two perovskite layers.<sup>[48]</sup> The compound is instable in air and decomposes within a few months. In Sr<sub>4</sub>FeMoO<sub>8-δ</sub>, perovskite-like blocks with a thickness of

two  $\text{BO}_6$  octahedra are separated by two rocksalt-like SrO layers.<sup>[40]</sup> A Ruddlesden–Popper phase formed in  $\text{Sr}_2\text{Fe}_{1+x}\text{Mo}_{1-x}\text{O}_6$  is  $\text{Sr}_3\text{Fe}_{5/4}\text{Mo}_{3/4}\text{O}_{6.9}$ , which also decomposes in the ambient (even in the glovebox) over a period of months.<sup>[50]</sup> The instability of SFMO Ruddlesden–Popper phases in humid conditions originates from the intercalation of two water molecules per formula unit forming a new  $\text{OH}^-/\text{H}_3\text{O}^+$  layer between two rocksalt layers.<sup>[51]</sup> SrO decomposes into  $\text{Sr}(\text{OH})_2$  when reacting with  $\text{CO}_2$  to form a carbonate.

First-principle calculations yield that the chemical bond of Sr is not affected by either ASDs or oxygen vacancies.<sup>[14]</sup>

### 2.3. Iron–Molybdenum Ratio

Recently, many efforts have been made to study the structural and magnetic properties of  $\text{Sr}_2\text{Fe}_{1+x}\text{Mo}_{1-x}\text{O}_6$ ,  $-1 \leq x \leq 1$ , compounds by varying Fe and Mo contents.<sup>[6,52–60]</sup> Fe and Mo nonstoichiometry in SFMO is mainly accommodated by forming  $\text{Fe}_{\text{Mo}}$  and  $\text{Mo}_{\text{Fe}}$  as AS defects.<sup>[6]</sup> Such AS defects create both Fe–O– $\text{Fe}_{\text{Mo}}$  and Mo–O– $\text{Mo}_{\text{Fe}}$  nearest-neighbor pairs, which affect the electronic and magnetic properties. Fe, replacing Mo sites in  $\text{Sr}_2\text{Fe}_{1+x}\text{Mo}_{1-x}\text{O}_6$ , reduces the total conduction electron density and thus weakens the double exchange mechanism,<sup>[61]</sup> which is responsible for ferromagnetic coupling.<sup>[58]</sup> Correspondingly,  $M_s$  deteriorates due to the ferrimagnetic spin state of Fe atoms on Mo sites.<sup>[6]</sup> On the other hand, a small amount of Mo vacancies in  $\text{SrFeMo}_{1-x}\text{O}_6$  (up to  $x = 0.4$ ) seems to improve the magnetic properties as shown in ref. [16]. At low concentrations ( $x \rightarrow 1$ ), Mo is in the  $\text{Mo}^{6+}$  state. With increasing Mo content, the Fe ion is reduced starting from  $\text{Fe}^{4+}$  and  $\text{Fe}^{3+}$  in  $\text{SrFeO}_{3-\delta}$  via an  $\text{Fe}^{3+}$  state to a mixture of  $\text{Fe}^{2+}$  and  $\text{Fe}^{3+}$  at  $x = 0.35$ .  $\text{Mo}^{5+}$  appears simultaneously with  $\text{Fe}^{2+}$ . Both reduced ions possess larger ion radii and form the driving force for a cubic to tetragonal lattice transformation between  $x = 0.35$  and  $0.50$ .<sup>[57]</sup> Experimentally, this phase transition was obtained already at  $x = 0.20$  in ref. [52] and at  $x \approx 0.35$  in ref. [55]. In stoichiometric SFMO, Mo was found in a mixed state ( $\text{Mo}^{6+}/\text{Mo}^{5+}$  in a 66%:34% ratio),<sup>[62]</sup> complementary to the  $\text{Fe}^{2+}/\text{Fe}^{3+}$  state.<sup>[37,63,64]</sup> Thus, SFMO can be considered to be in a  $\text{Fe}^{2+} + \text{Mo}^{6+} \leftrightarrow \text{Fe}^{3+} + \text{Mo}^{5+}$  mixed valence state. A further increase of  $x$  reduces molybdenum to  $\text{Mo}^{4+}$  for  $x \rightarrow -1$ .

In  $\text{Sr}_2\text{Fe}_{1+x}\text{Mo}_{1-x}\text{O}_6$  with  $x < 0$ , excess Mo increases the conduction electron density, diluting the ferromagnetic bonds.<sup>[58]</sup> The tetragonal structure was obtained to be stable for Fe deficiencies in the range of  $x = 0 \dots -0.1$ .<sup>[60]</sup> However, magnetic properties, especially LFMR, were found to be degraded. Surprisingly, also here, an improvement of magnetic properties of  $\text{Sr}_2\text{Fe}_{1-x}\text{MoO}_6$  compounds was obtained in a decreasing-increasing-decreasing behavior for a small Fe deficiency ( $x = 0.05$ ). Upon increasing the Mo-excess in  $\text{Sr}_2\text{Fe}_{1+x}\text{Mo}_{1-x}\text{O}_6$ , the half-metallic character of the compound predicted by first-principle calculations is lost at  $x \approx -0.125$ , that is, the compound resembles nonmagnetic strontium molybdate.<sup>[6]</sup>

For  $\text{Sr}_2\text{Fe}_{1+x}\text{Mo}_{1-x}\text{O}_6$  compounds, it has been found that the values of  $S$ ,  $M_s$ , and MR are highest at  $x = 0$  and are decreasing as  $x$  deviates from 0.<sup>[6,52–54,56,58,59]</sup>

The predicted spin polarization decreases with ASD and nonstoichiometry, in the latter case moderate at Mo-excess

( $x = -0.25$ ), but drastically at Fe-excess ( $x = 0.25$ ).<sup>[54]</sup> According to ref. [6], full spin polarization extends into the Mo-rich region up to  $x \approx -0.125$ , which means that a slight Mo-excess in thin films may not be harmful for device application.

### 2.4. Antisite Defects and Antisite Disorder

In accordance with a low AS defect formation energy,<sup>[5]</sup> Fe/Mo nonstoichiometry in SFMO is mainly accommodated by Fe and Mo AS defects, that is, by Fe atoms on Mo sites and vice versa. A crude estimation of the lower energy limit for the formation of lattice defects in a cubic crystal consisting of an A-atom in a host position B may be given by the elastic energy required for a volume change  $\Delta V \approx 3/2\Delta r$ :

$$\Delta H_f(A_B) = \left( \frac{3}{8}(c_{11} + 2c_{12}) + \pi(c_{11} - c_{12}) \right) a(\Delta r)^2 \quad (3)$$

where  $c_{ij}$  are elastic constants,  $a$  the lattice constant, and  $\Delta r$  the difference of the ion radii of the host and impurity atoms.<sup>[65]</sup> Inserting elastic constants from first-principle calculations in ref. [5] and  $\Delta r$  values between  $\text{Fe}^{2+}$  and  $\text{Mo}^{6+}$  ions taken from ref. [66] resulted in  $\Delta H_f(\text{Fe}_{\text{Mo}}) = \Delta H_f(\text{Mo}_{\text{Fe}}) = 0.22$  eV. On the other hand,  $\text{ABO}_3$  energetics are controlled mainly by the Goldschmidt tolerance factor<sup>[67,68]</sup>

$$t = \frac{d_{\text{A-O}}}{\sqrt{2}\langle d_{\text{B-O}} \rangle} \quad (4)$$

where the atomic distances,  $d$ , to the nearest oxygen neighbor are easily obtained by the Rietveld refinement method. Here,  $\langle \rangle$  stands for the average of B' and B'' parameters.<sup>[69]</sup> For nonstoichiometric samples, the tolerance factor can be adapted as proposed in ref. [16]. A reasonable estimation of the antisite defect formation energy is then given by

$$\Delta H_f(A_B) = \frac{\partial H_f(\text{ABO}_3)}{\partial t} (t_{\text{AB}'\text{O}_3} - t_{\text{AB}''\text{O}_3}) \quad (5)$$

with  $\partial H_f(\text{ABO}_3)/\partial t \approx 920$  kJ mol<sup>-1</sup> for  $\text{SrMO}_3$  (M = lanthanide or actinide) perovskites.<sup>[68]</sup> Note that this kind of estimations depends much on ion radii. We use Shannon's values taken from ref. [66] yielding an AS defect formation energy of 0.27 eV. First-principle calculations for a  $\text{Sr}_8\text{Fe}_4\text{Mo}_4\text{O}_{24}$  supercell results in ASD formation energies of about 0.4...0.7 eV, where ASD along the diagonal of the cubic B-site sublattice is predicted to be the most favorable while the formation energies of ASDs along the  $x$ – $y$  plane and  $z$  directions are very similar.<sup>[14]</sup> Another value of 0.77 eV was derived using the first-principle approach for AS  $\text{Mo}_{\text{Fe}} + \text{Fe}_{\text{Mo}}$  pairs in stoichiometric SFMO.<sup>[5]</sup> It is independent of oxygen partial pressure. On the other hand, the value of  $\Delta H_f(\text{Fe}_{\text{Mo}} + \text{Mo}_{\text{Fe}})$  in stoichiometric SFMO depends not only on the amount of disorder but also on the nearest-neighbor arrangement.<sup>[6]</sup> For SFMO exhibiting an ASD of 0.125, less energy (0.25 eV in the relaxed case) is needed for AS pair formation when they are placed next to each other than for the case with a third-nearest-neighbor arrangement (0.74 eV).

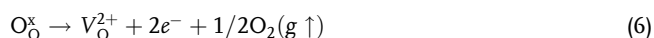
ASD in SFMO is lowest at an optimum synthesis temperature, which amounts to about 1200 °C for ceramics long-term

annealed under oxygen-deficient conditions,<sup>[70]</sup> and to about 850 °C for SFMO thin films deposited by PLD.<sup>[71]</sup> The maximum order indicates that a thermodynamic equilibrium is reached. Below the optimum temperatures, ASD is controlled by kinetics<sup>[70]</sup> and it increases with decreasing synthesis temperature.<sup>[57,72,73]</sup> The latter is a big challenge for thin film deposition at substrate temperatures that are compatible with silicon technology.

## 2.5. Oxygen Vacancies

Oxygen vacancies may be formed in two nonequivalent positions, in-plane ( $O_{xy}$ ) and out-of-plane ( $O_z$ ). The formation of oxygen vacancy ( $V_O$ ) implies a reduction of the other remaining species, that is, the oxidation state (the positive charge) of cations decreases. As a consequence, the ionic radii of Fe and Mo ions increase.<sup>[66]</sup> This alters the number of delocalized electrons and also affects the magnitude of magnetic moments of surrounding atoms. Additionally, electronic conductivity is enhanced upon oxygen vacancy formation through changes in  $d$ -state occupation.

The variation of the oxygen deficiency parameter  $\delta$  of  $Sr_2FeMoO_{6-\delta}$  depending on oxygen partial pressure is attributed to a  $V_O$  formation according to the defect reaction<sup>[27]</sup>



Oxygen nonstoichiometry  $\delta$  can be derived from the law of mass action and the electroneutrality condition

$$\delta = [V_O^{2+}] \sim p_{O_2}^{-n} \quad (7)$$

with  $n = 1/2$ . In this context, it has to be noted that 1 at% of oxygen vacancies corresponds to  $\delta = 0.06$ . The exponent  $n$  obtained in the temperature region from 1000 to 1200 °C within the stability region of SFMO amounts to 0.35,<sup>[27]</sup> illustrating that Equation (6) is a simplified picture of oxygen nonstoichiometry formation. A more precise model should include changes of the oxidation state of the two transition metal ions, reducing the number of delocalized electrons as well as vacancy interaction into Equation (6), for example, by overlapping local lattice deformations around the vacancy. According to first-principle calculations,<sup>[11]</sup> only 1.5 electrons on average are delocalized or localized on other atoms by removing one oxygen atom per cell. In the presence of AS defects where Fe-O- $Fe_{Mo}$  and Mo-O- $Mo_{Fe}$  nearest-neighbor pairs appear, a significant amount of electron density (0.4 e) delocalizes in the first case onto the oxygen sublattice. This delocalization reduces electronic repulsion and stabilizes the vacancy. In the second case, the electrons donated by the vacancy remain localized among the neighboring Mo atoms, leaving the rest of the electronic density almost unchanged.<sup>[14]</sup>

The value of  $\delta$  was determined only in a few number of reports.<sup>[27,74–77]</sup> SFMO ceramics synthesized using  $SrCO_3$ ,  $Fe_2O_3$ , and  $MoO_3$  powders as starting materials and applied to SFMO ceramics sintered at 1150 °C for 50 h in sealed ampoules together with Fe grains as oxygen trap possess an oxygen deficiency of  $\delta \approx 0.03 \pm 0.02$  as obtained by a redox method based on coulometric titration of both  $Fe^{2+}$  and  $Mo^{5+}$  in an inert Ar atmosphere.<sup>[74,78]</sup> In ref. [75], the reduction of  $M_S$  of SFMO by 1.8  $\mu B/f.u.$  was explained by a hypothesized value of  $\delta = 0.36$ .

The ceramic sample was synthesized from  $SrCO_3$ ,  $MoO_3$ , and  $Fe(C_2O_4) \cdot 2H_2O$  and subsequently sintered for 2 h at 900 °C. Values of  $\delta$  in the range from 0.0055 to 0.0913 (with a lower phase boundary  $\delta = 0.085$  at 1200 °C) were obtained for SFMO ceramics prepared with a standard mixed oxide route. By calculating at a given oxygen partial pressure, the change of oxygen nonstoichiometry is given by<sup>[26]</sup>

$$\Delta\delta = (\Delta m M_{SFMO} / \Delta m_0 M_O) \quad (8)$$

with  $m_0$  as initial sample mass and  $M$  as molar mass of SFMO and oxygen, respectively. For the calculation of  $\delta$ , the resulting  $\Delta\delta$  were fitted to the equation

$$\Delta\delta = \delta - \delta_0 = k p_{O_2}^{-n} - \delta_0 \quad (9)$$

where  $\delta_0$  is nonstoichiometry at the reference oxygen partial pressure,  $k$  an equilibrium constant, and  $n \approx 0.35$ . All parameters have been determined experimentally.<sup>[27]</sup> Iodimetry was performed by dissolving the sample in a dilute solution of HCl and  $I^-$  ions, and the quantity of  $I_2$  formed by oxidation was determined using titration of  $Na_2S_2O_3$ . This revealed values of  $\delta = 0.132$  and 0.296 for polycrystalline ceramic samples sintered in a flow of 5%  $H_2/Ar$  gas mixture at 1160 °C for 9 and 15 h, respectively.<sup>[76]</sup> By means of weighing the samples before and after their complete reduction in a hydrogen flux at 1100 °C for 20 h, values of  $\delta = 0.03 \dots 0.06$  were obtained in polycrystalline SFMO samples prepared by the solid-state synthesis technique from  $SrFeO_{2.52}$  and  $SrMoO_4$  precursors and annealed in a flux of 5%  $H_2/Ar$  gas mixture at 1150 °C for 5 h with a subsequent quenching to room temperature.<sup>[77]</sup>

Ceramic SFMO samples synthesized at 1150 °C for 50 h possess an oxygen vacancy concentration of 0.5%.<sup>[74]</sup> With regard to a quite small contribution of the first-principles-derived vibrational entropy to the Gibbs vacancy formation free energy of  $SrCoO_{3-\delta}$  and  $La_{0.5}Sr_{0.5}Mn_{0.5}Co_{0.5}O_{3-\delta}$  perovskite thin films,<sup>[79]</sup> we have to take into account only the entropy difference between oxygen ions in the solid and oxygen in the gas phase, which amounts to about 10  $k$  per O atom.<sup>[80]</sup> Here,  $k$  denotes the Boltzmann constant. Neglecting the small configurational entropy contribution, the enthalpy (internal energy) of oxygen vacancy formation  $H_f(V_O)$  yields about 1.88 eV. This value is significantly lower than the formation energies of neutral oxygen vacancies  $E_f(V_O)$  calculated from first principles.<sup>[13,14,81]</sup> For different configurations, the enthalpy values range from about 3 to about 6 eV at 0 K and 0 pressure. The thus-calculated values of  $E_f(V_O)$  are affected by the choice of chemical potential  $\mu_O$  of oxygen, which is known merely approximately for the given experimental conditions. Usually, oxygen-rich conditions are considered where an upper limit of  $\mu_O$  is chosen as half of the total energy of a free, isolated  $O_2$  molecule in the triplet state at  $T = 0$  K.<sup>[82]</sup> However, this upper limit can never be realized experimentally. On the other hand, the exact oxygen partial pressures in the fabrication processes of thin-film and bulk samples cannot be determined accurately, but their difference in film and bulk sample fabrication should be rather small.

However, introducing this in a combined DFT and thermodynamic model, and using a temperature- and partial pressure-dependent value  $\mu_O(T, p_{O_2})$ ,<sup>[82]</sup>  $E_f(V_O)$  values are reduced from

$\approx 4.5$  eV in the oxygen-rich limit to  $\approx 2.9$  eV at  $p_{O_2} = 2.1 \cdot 10^4$  Pa (corresponding to air) and to  $\approx 1.7$  eV at  $p_{O_2} \approx 10^{-4}$  Pa (corresponding to an atmosphere of ultrapure [99.9999%] Ar at 10 Pa).<sup>[5]</sup> In this model, oxygen nonstoichiometry vanishes in the oxygen-rich limit, but is still negligible,  $\delta \approx 10^{-4}$ , under low-pressure ultrapure Ar conditions. Another drawback of DFT is supercell finite-size errors. To save computation time, supercells are considered to be consisting of only two or four formula units. In this case, on-site Coulomb repulsive interaction cannot be properly taken into account.<sup>[7]</sup> A supercell of four-formula units should be a minimum size.<sup>[6]</sup> When using DFT + U calculations,<sup>[6,7,13,14,81,83]</sup> the strengths of on-site interactions are usually described by a parameter

$$U_{\text{eff}} = U - J \quad (10)$$

which is the difference between the average Coulomb energy and the exchange energy. Thereby,  $d$  and  $f$  electrons in magnetic systems can be properly modeled. Unfortunately, there is no consistent procedure for the determination of  $U_{\text{eff}}$ . The parameters  $U$  and  $J$  are obtained either semi-empirically by choosing them in a way that the results coincide with the experimentally obtained structural or magnetic properties, or they are extracted from *ab initio* calculations, e.g., ref. [84]. Other uncertainties in modeling ionic defects using DFT are reviewed in ref. [85]. Experimentally, the partial molar enthalpy of oxygen was determined in the temperature region from 1140 to 1230 °C from the slope of the upper phase-stability line of SFMO in a  $p_{O_2}$  versus  $1/T$  diagram.<sup>[29]</sup> This quantity is equivalent to  $E_f(V_O)$ . It amounts to  $1.73 \pm 0.08$  eV in satisfactory agreement with first-principle calculations extended by thermodynamic considerations of the chemical potential of oxygen.<sup>[5]</sup>

In cubic  $\text{SrFeO}_{3-\delta}$ , the oxygen vacancy formation energy exhibits a constant low value ( $\approx 0.4$  eV) for  $\delta < 0.05$ ; increases to  $\approx 0.5$  eV for  $0.05 < \delta < 0.1$ ; and further increases quickly with concentration when  $\delta > \approx 0.1$ .<sup>[86]</sup> This increase is attributed to the local charge redistribution after  $V_O$  formation and to overlapping local lattice transformations. By the same reason, the dependence of SFMO oxygen diffusion activation energy on oxygen nonstoichiometry<sup>[87]</sup> provides evidence of vacancy interactions over distances at least up to four unit cells. A similar oxygen diffusion behavior was found earlier for  $\text{SrCo}_{0.8}\text{Fe}_{0.2}\text{O}_{3-\delta}$  ceramics<sup>[88]</sup> and for PLD  $\text{Ba}_{0.5}\text{Sr}_{0.5}\text{Co}_{0.8}\text{Fe}_{0.2}\text{O}_{3-\delta}$  thin films,<sup>[89]</sup> but at much higher oxygen deficiencies, that is, much lower interaction distances.

With regard to their small formation energy, AS defects are the most abundant point defects in stoichiometric SFMO. Moreover, oxygen deficiency is correlated with ASD (Figure 4).

According to Figure 4, SFMO saturated with oxygen ( $\delta \rightarrow 0$ ) exhibits a base level of about 5% of AS defects, which is in good agreement with experimental data in ref. [52,63,91,92]. The slope of Figure 4 yields a correlation of each oxygen vacancy with about two AS defects. This suggests the conclusion that oxygen vacancies are interacting via AS defects. The appearance of AS defects generates both Fe-O- $\text{Fe}_{\text{Mo}}$  and Mo-O- $\text{Mo}_{\text{Fe}}$  nearest-neighbor pairs. The formation energies of oxygen vacancies are for their part very sensitive to the nearest-neighbor arrangement. For instance, the formation energy for oxygen vacancies along Fe-O- $\text{Fe}_{\text{Mo}}$  bonds is predicted to be  $\approx 1$  eV lower in energy than

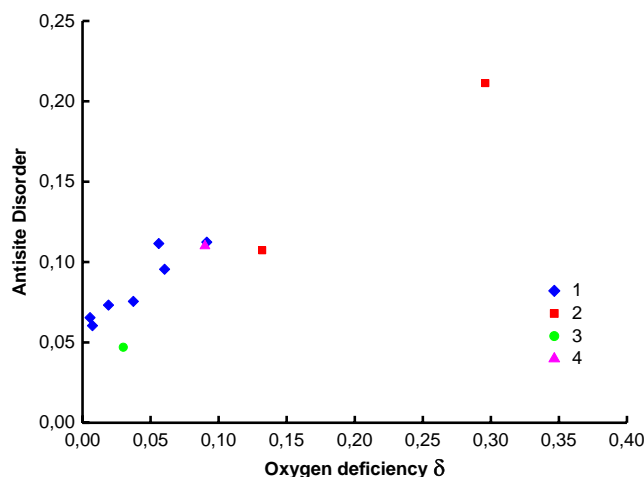


**Figure 4.** ASD in dependence on oxygen deficiency  $\delta$ . Data from: 1, ref. [27]; 2, ref. [76]; 3, ref. [78]; and 4, ref. [90].

the Fe-O- $\text{Mo}_{\text{Fe}}$  one in defect-free SFMO.<sup>[14]</sup> Early-transition metals such as Mo bind much more strongly to oxygen than late-transition metals such as Fe.<sup>[93]</sup> Consequently, a significant amount of electron density delocalizes in the Fe-O- $\text{Fe}_{\text{Mo}}$  case onto the oxygen sublattice and stabilizes the vacancy. As a result, the presence of ASD promotes oxygen vacancy formation. Note that further oxidizing a stoichiometric sample at a low temperature of 400 °C with an oxygen partial pressure of 6 Pa up to  $\delta = -0.04$  localizes oxygen near the surface of the grains and generates a small amount of a  $\text{SrMoO}_4$  impurity phase, which improves LFMR, but does not diminish  $M_s$ .<sup>[94]</sup>

Contrarily to the view in this section, oxygen deficiencies  $\delta$  were found to induce a superstructural ordering for samples with  $\delta = 0.03 \dots 0.06$ .<sup>[77]</sup> However, XRD with superstructure peaks of different intensity were not related by the authors to a particular oxygen deficiency.

## 2.6. Strained Films

Complex oxides are mostly applied as thin films. Therefore, biaxial strain induced due to lattice mismatch,<sup>[95,96]</sup> different thermal expansion coefficients upon cooling from the growth temperature,<sup>[97]</sup> or cationic or oxygen off-stoichiometry<sup>[98]</sup> have to be taken into account. Film strain is more significant for thin films below a critical thickness.

SFMO films deposited onto  $\text{SrTiO}_3(001)$ <sup>[99,100]</sup> and  $\text{MgO}(001)$  substrates<sup>[99]</sup> grow in the Stranski-Krastanov mode.<sup>[101]</sup> Initially, one or more monolayers are grown in a layer-by-layer fashion. Beyond a critical layer thickness, which depends on strain and substrate nature, growth continues through nucleation and coalescence of islands, relieving film strain. In a layer-by-layer epitaxially grown thin film, the in-plane lattice parameter of very thin films is close to the one of the substrate.<sup>[102]</sup> Therefore, SFMO thin films sustain in-plane compressive strain when deposited onto substrates with a smaller lattice parameter, e.g.,  $\text{SrTiO}_3(001)$ , and in-plane compressive strain on substrates with a larger one such as  $\text{MgO}(001)$ .<sup>[103]</sup> The out-of-plane lattice parameter results from an unconstrained minimization of

atomic forces. It is usually expanded with respect to bulk value regardless of the sign of lattice mismatch of the substrate<sup>[104]</sup> and decreases toward the bulk value with increasing growth temperature and decreasing deposition rate.<sup>[96]</sup> With the increase of film thickness, strain in the SFMO thin film becomes relaxed toward the bulk lattice parameter values.<sup>[96,102,105]</sup> A general trend in SFMO films is that the smaller the lattice parameter, the better the magnetic film properties.<sup>[104]</sup> Strain relaxation of SFMO thin films on SrTiO<sub>3</sub>(001) occurs in the range of 30–80 nm.<sup>[97,102]</sup>

The relaxation of SFMO thin films occurs through stacking faults, which are perpendicular to the surface of the substrate and originate from the SFMO/substrate interface.<sup>[97]</sup> Another effective mechanism for the relief of compressive strain is the formation of secondary phase, e.g., SrMoO<sub>3</sub>,<sup>[99,103]</sup> allowing the SFMO film lattice parameters to more closely approach those of bulk SFMO. A mechanism for the relaxation of tensile strain is the formation of a Fe-rich layer at the substrate/film interface.<sup>[105]</sup> Octahedra rotation is an additional mechanism for the compensation of both tensile and compressive in-plane biaxial strain.<sup>[106]</sup> The rotation becomes larger under compressive biaxial strain.<sup>[5]</sup>

At a large negative lattice mismatch, e.g., for LaAlO<sub>3</sub>(001) substrates,<sup>[99]</sup> the growth modes change from Stranski–Krastanov to Volmer–Weber mode.<sup>[107]</sup> The latter is characterized by a 3D growth of isolated islands at the initial state, since the adatom–adatom interactions are stronger than those of the adatom with the surface. With island coalescence, the interfacial energy is reduced at the expense of associated strain energy of the stretching toward each other island forming a grain boundary.<sup>[108]</sup> This compensates in part the large lattice mismatch.

To explain the effect of strain on the magnetic properties of SFMO films deposited onto different substrates, oxygen vacancies need to be considered.<sup>[109]</sup> Since the unit cell volume increases with tensile strain and decreases with compressive one, V<sub>O</sub> formation energy is sensitive to the biaxial strain induced on a substrate–thin film interface. The reduction Fe and Mo ions by oxygen vacancy formation increase their ionic radii.<sup>[66]</sup> The results of first-principle calculations are not consistent. With compressive strain, vacancy formation energies were predicted to increase in ref. [13], and to decrease in ref. [5]. The higher T<sub>C</sub> and reduced M<sub>s</sub> in tensile-strained films suggest that tensile strain and interface defects promote the formation of oxygen vacancies.<sup>[110]</sup> According to ref. [5], the formation energies of in-plane (O<sub>xy</sub>) and out-of-plane (O<sub>z</sub>) vacancies decrease differently in dependence on both tensile and compressive biaxial strain. For compressive strain, this effect is less pronounced for V<sub>Oz</sub> vacancies and smaller than for tensile strain. Thus, the formation of oxygen vacancies is more likely for tensile strain. The same was obtained for CaMnO<sub>3</sub> with a more pronounced effect for V<sub>Oxy</sub> vacancies.<sup>[106]</sup> The higher amount of oxygen vacancies in tensile-strained samples causes a higher T<sub>C</sub> compared to the compressively strained ones (cf. Section 3.2).

The formation energies of antisite defects increase within a strain range of ±3%. Thus, the amount of antisite disorder can be reduced by means of strain to obtain improved magnetic properties of SFMO. First-principle GGA+U calculations in ref. [13] revealed an increase of AS defect formation energies, that is, the SFMO lattice is stabilized against AS formation. Contrarily, compressive strain was found to reduce the antisite

disorder favoring device application in spintronics,<sup>[5,13]</sup> but also to increase ASD thereby decreasing magnetization.<sup>[96]</sup> Experimentally, a decrease of compressive strain by means of a Ba<sub>0.4</sub>Sr<sub>0.6</sub>TiO<sub>3</sub> buffer layer has been found to improve M<sub>s</sub>.<sup>[111]</sup>

Considering the other point defects, V<sub>Sr</sub>, V<sub>Fe</sub>, and Mo<sub>Fe</sub> are marginally influenced by biaxial strains in the range from –3% to 3%.<sup>[5]</sup>

First-principle calculations<sup>[13]</sup> predict that even large lattice strains maintain the half-metallic character of SFMO. On the other hand, an earlier study<sup>[97]</sup> suggests that very thin films matched to the lattice parameter of SrTiO<sub>3</sub> (lattice parameter >0.556 nm) are theoretically nonhalf-metallic, that is, it does not seem possible to obtain fully strained half-metallic ultrathin films.

To reduce strain, the substrate is usually chosen to have lattice parameters close to the desired film material.<sup>[104,111]</sup> Compressive biaxial strains of about –1% at strontium titanate substrates do not show any significant direct impact on the magnetic properties of SFMO.<sup>[13]</sup> Consequently, a small negative lattice mismatch will not be a disadvantage, because strain can be beneficial for the magnetic properties, enhancing saturation magnetization via a diminution of antisite disorder.

Substrates suitable for a silicon-based technology are both (100)-oriented silicon (lattice misfit –2.7%<sup>[112]</sup>) and platinized silicon wafers exhibiting a (111) texture (lattice misfit estimated as –1.7%). In the first case, problems arise at the interface by the strong oxidizing action of SFMO. On the other hand, due to a different nucleation and growth mechanism, (111)-oriented films possess a mosaic texture exhibiting the potential of a larger LFMR.

Strain can be tuned by varying the substrate,<sup>[110]</sup> using different buffer layers<sup>[113]</sup> or by changing the thickness of the film.<sup>[97]</sup> By tuning the level of strain from compressive to tensile with the use of different buffer layers, switching of magnetocrystalline anisotropy from an in-plane to an out-of-plane state has been demonstrated in SFMO thin films.<sup>[114]</sup>

### 3. Effect of Point Defects on Saturation Magnetization, Curie Temperature, and Low-Field Magnetoresistance

Avoiding deterioration of thin film properties in comparison with the bulk is extremely challenging. Although SFMO is a promising candidate for magnetic device applications, currently no thin film synthesis technique is known that would preserve the magnetic properties of bulk SFMO.<sup>[13]</sup> Thin films are synthesized at much lower temperatures than bulk ceramics. This leads inherently to a larger ASD.<sup>[57,72,73]</sup> In most cases, M<sub>s</sub> and T<sub>C</sub> values of thin films are lower than for the bulk.<sup>[71,111,115–117]</sup> The magnetoresistance of SFMO thin films at room temperature has not exceeded a few percentage,<sup>[32,118,119]</sup> and is much lower than the magnetoresistances of bulk materials, which reach a value as high as 11%.<sup>[120,121]</sup> A direct comparison of SFMO thin films fabricated by PLD on SrTiO<sub>3</sub>(001) substrates and a polycrystalline SFMO target used in film deposition was reported in ref. [13]. T<sub>C</sub> of the standard 160-nm-thick SFMO film was found to be around 320 K, whereas that of a polycrystalline bulk material was 23% higher, while M<sub>s</sub> of the film was 33% higher than

in the bulk sample. The large difference in Curie temperature and saturation magnetization between SFMO thin films and polycrystalline bulk sample was related to antisite disorder and oxygen vacancies. Thus, for a deeper understanding of film peculiarities, an examination of the effects of antisite disorder and oxygen vacancies is necessary. Since SFMO thin film applications would benefit from the low-field magnetoresistance, Section 3.4 analyzing this property was included for completeness.

A first-principle study of defective SFMO reveals that (except Sr vacancies) all other point defects (Mo, Fe and oxygen vacancies,  $\text{Fe}_{\text{Mo}}$  and  $\text{Mo}_{\text{Fe}}$  antisites, as well as  $\text{Fe}_{\text{Mo}} + \text{Mo}_{\text{Fe}}$  pairs) degrade the total magnetic moment  $\mu_{\text{tot}}$ .<sup>[7]</sup> The reason for this slight increase in the  $V_{\text{Sr}}$  case was attributed both to the slightly larger parallel aligned (positive) magnetic moment of four Fe atoms, that is slightly larger for perfect SFMO, and the slightly larger antiparallel-aligned (negative) magnetic moment for four Mo atoms. Degradation occurs with increasing ASD for saturated magnetization with stoichiometries deviated from Fe/Mo stoichiometry as well as for spin polarization as a function of ASD in stoichiometric SFMO.<sup>[6]</sup>

### 3.1. Saturation Magnetization

The correlation between  $M_s$  and ASD defects has been widely studied.<sup>[8,11,13,17,27,53,72–75,90,91,94,122–128]</sup> The degradation of both  $M_s$  and  $T_C$  with increasing ASD as well as the degradation of  $M_s$  with increasing concentration of oxygen vacancies were predicted in ref. [8] based on Monte Carlo simulation. The correlation between  $M_s$  and  $T_C$  deterioration was later experimentally confirmed in ref. [73]. **Figure 5** illustrates the effect of oxygen deficiency on saturated magnetization of SFMO.

Experiments have shown a decrease in  $M_s$  with deviation from Fe/Mo stoichiometry,<sup>[53]</sup> an decrease in  $M_s$  and  $T_C$  with ASD in SFMO single crystals<sup>[17]</sup> as well as in SFMO ceramics,<sup>[123]</sup> a decrease in  $M_s$  with simultaneously increasing ASD and oxygen

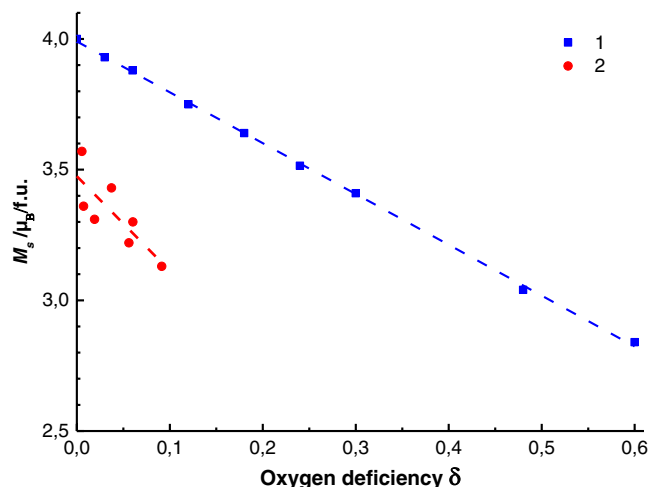


**Figure 5.** Influence of oxygen nonstoichiometry on saturation magnetization  $M_s$  calculated by a first-principle approach (1) (data from ref. [122]) and compared to the experimentally observed combined effect of ASD and oxygen vacancies on  $M_s$  (2) (data from ref. [27]).

vacation concentration,<sup>[27]</sup> and a diminution of spin polarization with ASD.<sup>[90]</sup> On the other hand, Sr off-stoichiometry enhances ASD both in Sr-deficient and Sr-excess samples, deteriorating saturation magnetization (cf. **Table 1** in ref. [13]).

Assuming equilibrium conditions and reasonable oxygen partial pressures, AS defects and oxygen vacancies appear to be the most abundant point defects in SFMO.<sup>[5]</sup> By removing one  $\text{O}^{2-}$  ion from the lattice, the total magnetic moment in the unit cell will be reduced by about  $2 \mu_B$ .<sup>[11]</sup> On the other hand, a pair of an oxygen vacancy and a  $\text{Fe}_{\text{Mo}}$  AS reduce  $\mu_{\text{tot}}$  by  $8 \mu_B$ <sup>[124]</sup>—not distinguishable from the contribution of an AS alone.<sup>[72]</sup> Since vacancies favor atomic mobility, it is reasonable to assume that  $\text{V}_{\text{O}}\text{-Fe}_{\text{Mo}}$  pairs are formed. As a result, the formed Fe-O- $\text{Fe}_{\text{Mo}}$  bonds strongly favor a parallel coupling between the magnetic moments of Fe atoms.<sup>[11]</sup> The formation energy of oxygen vacancies for Fe-O- $\text{Fe}_{\text{Mo}}$  bonds, calculated by first principles is smallest, that is, about 1 eV lower in energy than the one for Fe-O-Mo bonds in defect-free SFMO.<sup>[14]</sup>

Saturation magnetization decreases linearly with the Mo/Fe antisite defect concentration  $x$ <sup>[8]</sup>

$$M_s = M_s(\text{ASD} = 0) - b\text{ASD}(\mu_B/\text{f.u.}) \quad (11)$$

where the coefficient  $b$  depends on the nature of magnetic coupling between metal cations,<sup>[125]</sup> the competition of magnetic moments on ions in antisite positions, the relative orientation between Fe moments at antisite positions and Fe moments on the regular sites,<sup>[75]</sup> and the additional presence of oxygen vacancies.<sup>[11]</sup> Another factor lowering the experimental  $M_s$  values is the presence of grain and antiphase boundaries.<sup>[94,126,127]</sup> The values of  $b$  range between  $6.56$ <sup>[11,75]</sup> and  $10$ .<sup>[72,91,125]</sup>

A suitable approximation is the ferromagnetic arrangement (FIM) model<sup>[72]</sup> where  $\text{Fe}^{3+}(3d^5, S = 5/2)$  ions in B-sites are antiferromagnetically coupled to its six  $\text{Mo}^{5+}(4d^1, S = 1/2)$  neighbors occupying the B' sites. This approach is in good agreement with experimental data.<sup>[17,72,75,92,103,128]</sup> This ideal arrangement produces a net magnetization of

$$M_s = (1 - 2\text{ASD})m_{\text{Fe}} - (1 - 2\text{ASD})m_{\text{Mo}} \quad (12)$$

where  $m_{\text{Fe}}$  and  $m_{\text{Mo}}$  are the magnetic moments of Fe and Mo ions, respectively. Assuming a spin-only contribution with  $m_{\text{Fe}}(\text{Fe}^{3+}) = 5 \mu_B$  and  $m_{\text{Mo}}(\text{Mo}^{5+}) = 1 \mu_B$ , we arrive at  $M_s(\text{ASD} = 0) = 4 \mu_B/\text{f.u.}$  and  $b = 8$ . Thus, the FIM model is a simple mean-field model that omits the itinerant character of spin-down electrons for the sake of simplicity. This simplified approach allows also an estimate of the effect of other point defects on  $M_s$ . Sr deficits without the formation of oxygen vacancies lead to an increase of the valence of the Fe-Mo couple. According to the FIM model, this is fully borne by Mo ions. This transfers Equation (11) into:<sup>[12]</sup>

$$M_s = 4 + \Delta - (8 + 2\Delta)\text{ASD}(\mu_B/\text{f.u.}) \quad (13)$$

where  $\Delta$  represents the increase of molybdenum valence ( $\Delta = 2x$  where  $x$  is the concentration of strontium vacancies in  $\text{Sr}_{2-x}\text{FeMo}_{6-\delta}$ ). Since a small excess  $x$  of Sr is accommodated by the formation of  $\text{V}_{\text{Mo}}$  (cf. Section 2.2), yielding a compound  $\text{Sr}_2\text{FeMo}_{1-x}\text{O}_6$ , Equation (11) changes in the absence of  $\text{V}_{\text{O}}$  formation and AS redistribution as

**Table 1.** Synthesis parameters and LFMR properties of ceramic SFMO composites.

Synthesis method	Sintering temperature [°C]	Sintering duration [min]	Sintering atmosphere	Composite phase	MR, @0.2T [%]	T [K]	Ref.
SSR <sup>a)</sup>	430	20	5%H <sub>2</sub> /N <sub>2</sub>	50% Pb-Si-B glass	-18	10	[155]
SSR	430	20	36%H <sub>2</sub> /N <sub>2</sub>	50% Pb-Si-B glass	-17	10	[127]
Sol-gel + powder	600	30	5%H <sub>2</sub> /N <sub>2</sub>	30% CeO <sub>2</sub>	-2.21	10	[156]
					-1.61	300	
SSR	1200	120	5%H <sub>2</sub> /Ar	15% Zn <sub>x</sub> Fe <sub>1-x</sub> Fe <sub>2</sub> O <sub>4</sub>	-6,9	300	[121]

<sup>a)</sup>SSR, solid-state reaction.

$$M_s = 4 + x - 8ASD(\mu_B/f.u.) \quad (14)$$

In the presence of Mo- or Fe-excess, AS defects Mo<sub>Fe</sub> or Fe<sub>Mo</sub> appear besides the AS Mo<sub>Fe</sub> + Fe<sub>Mo</sub> pairs, that is, [Mo<sub>Fe</sub>] ≠ [Fe<sub>Mo</sub>]. Denoting the site occupation factors as O<sup>B'</sup> and O<sup>B''</sup>, for B' and B'' sublattices, respectively, Equation (11) should be written in the case of Mo deficiency as<sup>[16]</sup>

$$M_s = 4 + x - 10 \left[ O_{Fe}^{B''} + \left( 1 - O_{Fe}^{B'} - O_{Mo}^{B'} \right) \right] - 2O_{Mo}^{B'} (\mu_B/f.u.) \quad (15)$$

and in the case of Fe deficiency as

$$M_s = 4 - 5x - 10O_{Fe}^{B''} - 2 \left[ O_{Mo}^{B'} + \left( 1 - O_{Fe}^{B''} - O_{Mo}^{B''} \right) \right] (\mu_B/f.u.) \quad (16)$$

Note that ASD is defined only for a stoichiometric Fe/Mo ratio, that is, for O<sub>Fe</sub><sup>B'</sup> = O<sub>Mo</sub><sup>B'</sup>. In this case, all corrections to M<sub>s</sub> are small and Equation (11) represents a suitable approximation.

Saturation magnetization has been observed to decrease with increasing lattice mismatch.<sup>[99,129]</sup> Fully strained films exhibit low M<sub>s</sub> values. Increasing film thickness, a monotonic increase of M<sub>s</sub> of ≈1 μB/f.u. was observed with decreasing compressive in-plane strain.<sup>[13]</sup> With increasing film relaxation, saturation magnetization was claimed to both increase<sup>[96]</sup> and decrease,<sup>[130]</sup> the latter for Fe-rich SFMO films.

### 3.2. Curie Temperature

Strontium deficiency leads to a moderate increase in ASD and a significant decrease in Curie temperature T<sub>C</sub>.<sup>[12,38]</sup>

In Sr<sub>2</sub>Fe<sub>1+x</sub>Mo<sub>1-x</sub>O<sub>6-δ</sub>, T<sub>C</sub> exhibits a continuous increase between x = -0.2 and 0.1.<sup>[52]</sup> With further increase of x, T<sub>C</sub> exhibits a sharp drop around the phase transition point at x = 0.2. A step decrease in T<sub>C</sub> with increasing Mo-excess, x > 0.05, was reported also in ref. [53]. Curie temperature is almost insensitive to a small Fe-excess.<sup>[53,55,60]</sup>

Electron doping provides a strategy to enhance T<sub>C</sub>.<sup>[131]</sup> On the other hand, both strontium and molybdenum vacancies provide holes to the electronic system, hence decreasing T<sub>C</sub>.<sup>[16,38]</sup> The initial increase of T<sub>C</sub> up to ASD = 0.1 predicted in ref. [132] coincides with T<sub>C</sub> values in Sr<sub>2</sub>FeMo<sub>1-x</sub>O<sub>6-δ</sub> that are higher than that of undoped samples. The latter possess a maximum of both T<sub>C</sub> and M<sub>s</sub> at x = 0.04.<sup>[16]</sup> In this case, it has to be taken into

account that the maximum degree of ordering in Sr<sub>2</sub>Fe<sub>1+x</sub>Mo<sub>1-x</sub>O<sub>6-δ</sub> occurs at x = -0.05.<sup>[52]</sup>

Similar to saturation magnetization, Equation (11), the deterioration of T<sub>C</sub> with ASD can be described by<sup>[8]</sup>

$$T_C = T_C(ASD = 0) - bASD \quad (17)$$

Monte Carlo simulations yielded parameter values of T<sub>C</sub> (ASD = 0) = 456 K and b = 300 K obtained by ref. [8], which are in good agreement with experimentally determined values of T<sub>C</sub> (ASD = 0) = 422 K and b = 152 K for ASD < 0.16 obtained for SFMO single crystals.<sup>[17]</sup>

The dependence of Curie temperature on oxygen vacancy concentration is still under debate. Based on a first-principle study, oxygen vacancies are suggested to favor an increase of T<sub>C</sub> in SFMO, while the total magnetic moment is reduced.<sup>[122]</sup> A forthcoming study<sup>[13]</sup> supposes that, by increasing the number of oxygen vacancies, T<sub>C</sub> of SFMO can be increased without deteriorating its half-metallicity. The authors of ref. [77] attribute the elevation of T<sub>C</sub> to an increase of free-carrier concentration leading to a rise of the density of states at the Fermi level and, as a consequence, to an enhancement of exchange interaction. This explanation is in contradiction to ref. [122] where the introduction of oxygen vacancies was found to resemble a stronger localization of the orbitals leading to a decrease in electron hopping and, thereby, to a decrease in magnetic coupling strength. A strong connection of T<sub>C</sub> to the density of states at the Fermi level was proposed in ref. [133]. The strength of ferromagnetic coupling is thus controlled by carrier mobility in the conduction band and the density of charge carriers. This is the basis for the above-mentioned strategy to increase T<sub>C</sub> by electron doping.

Experimental evidence for an increase of T<sub>C</sub> with increasing V<sub>O</sub> concentration is given in ref. [13]. The authors compared two types of SFMO: i) a polycrystalline PLD target that was made by the citrate-gel method and ii) a thin film deposited by means of PLD onto SrTiO<sub>3</sub>(100) substrates. ASD of the polycrystalline material was found to be around 28%, which is at least twice as large as the 12% ± 3% of ASD in the films. Based on E<sub>f</sub>(V<sub>O</sub>) calculations, a lower amount of oxygen vacancies was expected in the films compared to the polycrystalline bulk. On the other hand, the T<sub>C</sub> value of 160-nm-thick SFMO films was found to be around 320 K, whereas T<sub>C</sub> of the polycrystalline bulk material was 23% higher, around 400 K. The large difference in T<sub>C</sub> between the target and the film was explained by the lower amount of V<sub>O</sub> in the film. A theoretical study in ref. [122] addresses explicitly the variation of T<sub>C</sub> with V<sub>O</sub>. The first-principle calculation of magnetic coupling

between the B-site ions reveals that the oxygen-mediated exchange between Fe ions reduces whereas the AFM exchange between Fe and Mo ions is favored. At the same time, the stronger AFM coupling between Fe and Mo sites will mediate an additional FM coupling and increases  $T_C$  while the total magnetic moment is reduced.

Contrarily, a decrease in  $T_C$  with increasing oxygen deficiency was experimentally confirmed in ref. [76]. However, ASD effects were not completely ruled out in this article.

With decreasing compressive biaxial in-plane (tensile out-of-plane) strain,  $T_C$  increases monotonously by a few Kelvin, while the half-metallic character is preserved for both compressive and tensile strains up to 3%.<sup>[13]</sup>

### 3.3. Spin Polarization

Spin polarization  $P$  of SFMO depends on the disorder on B-sites (the formation of antisite pairs consisting of Fe atoms on Mo sites [ $\text{Fe}_{\text{Mo}}$ ] and vice versa). A value of  $P = 0.4 \dots 0.75$  was stated within uncertainty of data analysis for highly ordered SFMO thin films in ref. [134]. For the SFMO layer in a SFMO/SrTiO<sub>3</sub>/Co junction, possessing a fraction  $S \approx 0.85 \dots 0.87$  of correctly located B' and B'' ions, spin polarization of 85% was deduced by means of the Jullière model.<sup>[135]</sup> According to the point contact Andreev reflection technique,  $P$  reaches 70% in single crystals of SFMO with an order parameter  $S = 0.89$  as evaluated using the Rietveld refinement method.<sup>[90]</sup>

### 3.4. Low-Field Magnetoresistance

A practical application of LFMO requires a substantial magnetoresistive effect at low magnetic fields from 100 to 200 mT. LFMR was discovered in 1998.<sup>[2]</sup> It has been reported to exist in polycrystalline samples in magnetic fields of 0...0.5 Tesla<sup>[136,137]</sup> and is almost absent in single crystals.<sup>[91]</sup>

At present, it is well established that in SFMO ceramics the main contribution to LFMR arises from spin-dependent electron tunneling across insulating grain boundaries (GBs)<sup>[94,128,137–140]</sup> and not by ASD.<sup>[141]</sup> ASD comes into play solely at high levels of  $\text{ASD} \geq 0.26$ .<sup>[128]</sup> In the case of a significant disorder,  $\text{ASD} = 0.3$ , LFMR diminishes only for low-resistivity films, that is, weak insulating barriers, while the effect of disorder is negligible when GBs dominate in transport properties.<sup>[139]</sup>

A study of an epitaxial SFMO thin film grown on a SrTiO<sub>3</sub>(100) bicrystal boundary gives evidence that LFMR is similar to ceramics and is caused by an electron spin-dependent transfer across GBs and not by an intragranular effect.<sup>[142]</sup> Depending on deposition conditions, LFMR might be missing in SFMO thin films deposited by PLD onto SrTiO<sub>3</sub>(001) substrates.<sup>[32,109]</sup> However, the tunneling barriers necessary for LFMR could be additionally created, for instance, by a post-deposition film annealing at 475–500 °C in an ultrapure Ar (99.9995%) atmosphere for 5 h<sup>[32]</sup> or by annealing in a reducing 5% H<sub>2</sub>/N<sub>2</sub> atmosphere for 10 h.<sup>[143]</sup> Contrarily, neither magnetic nor magnetotransport or structural properties were improved by postdeposition annealing of SFMO thin films between 500 and 1100 °C in vacuum, Ar, 5% H<sub>2</sub>/Ar, and air atmospheres for 5 or 10 h.<sup>[144]</sup> Obviously, grain boundary modification should

be performed under carefully selected conditions. LFMR is favored in thin films subjected to large biaxial compressive strain at the film–substrate interface.<sup>[109]</sup> This is attributed to the formation of low-angle GBs. SFMO thin films grown by PLD on SrTiO<sub>3</sub>(111) substrates exhibit a larger LFMR effect in (111)-oriented films compared to that ones with (001) orientation.<sup>[145]</sup> The origin of this phenomenon is suggested to be the presence of antiphase domain boundaries since the superstructure direction is aligned here to the growth direction.

LFMR can be significantly improved by modifying GB-insulating barriers by means of: 1) slightly oxidizing the sample to form SrMoO<sub>4</sub> as an impurity phase, strengthening the insulating barrier [Table S1 and S2, Supporting Information], 2) modification of GBs by A-site substitution,<sup>[146,147]</sup> Co doping,<sup>[148]</sup> as well as combining A-site substitution and doping,<sup>[149,150]</sup> 3) forming composites (Table 1), 4) reducing grain size in the nanometer range (Figure 6), 5) postsynthesis annealing,<sup>[138]</sup> etc.

The low temperature for oxidation in ref. [139] is not high enough to modify the SFMO bulk substantially. Thus, the SrMoO<sub>4</sub> phase is expected to be located at the GBs with the consequence of enhancing the intergrain insulating barrier. Oxygen cycling creates SrMoO<sub>4</sub> under oxidizing conditions and Fe<sub>2</sub>Mo as well as FeO under reducing conditions.<sup>[151]</sup> It changes the oxygen content not only in GBs but also in the bulk. Upon overoxidation, the SFMO intragranular regions become Fe-rich, and the intergranular regions Mo-rich. The Fe-rich material is required to compensate for the Mo-rich regions created at GBs. The highest LFMR value corresponds to the point in the oxidation–reduction cycle where SrMoO<sub>4</sub> just begins to appear or disappear. SrMoO<sub>4</sub> regions that are too thick will not act as effective tunnel barriers.<sup>[151,152]</sup> Excess Fe was obtained in large grains also in ref. [152]. The intensity of the superstructure peak (101) in XRD pattern gives evidence that these extra Fe ions lead to anti-ferromagnetic Fe-O-Fe interactions and produce antisite defects. On the other hand, LFMR diminishes in more Fe-deficient

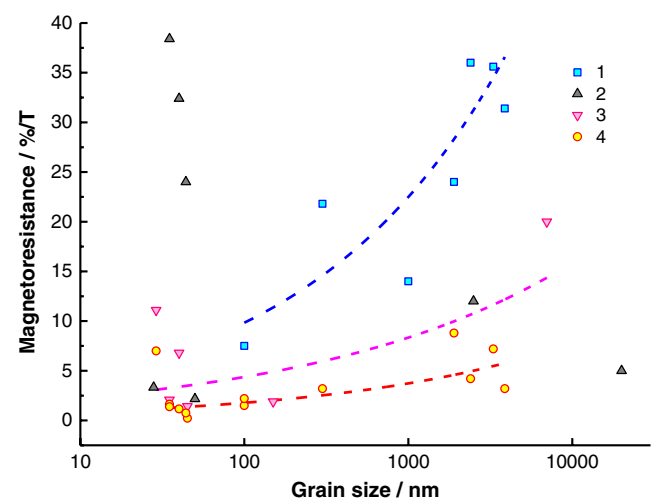


**Figure 6.** Relative change of magnetoresistance per magnetic flux density as a function of SFMO grain size. Data for SFMO ceramics were taken from refs. [96,151,174–176] and for SFMO thin films from refs. [117,119,140]. MR measured for  $H \leq 1$  T was classified into different temperature ranges: (1) 4–5 K, (2) 10–20 K, (3) 50–77 K, and (4)  $\approx 300$  K.

(>2%) SFMO ceramics since the reduction of Fe-O-Mo bonds degrades the LFMR properties, and the deficiency of Fe in Mo sublattice opens up Mo-to-Mo hopping channels via oxygen states, thereby reducing spin polarization.<sup>[60]</sup> Thus, large Fe deficiency is highly detrimental to attain suitable LFMR values in SFMO.

The SrMoO<sub>4</sub> phase in SFMO PLD thin films was studied also in other reports. In ref. [153], no MR data was specified for SrFeO<sub>3</sub> nanoparticles that were dispersed in SrMoO<sub>4</sub> grains although a FM hysteresis loop attributed to SrFeO<sub>3</sub> was present, while in ref. [154], MR data of an SFMO film consisting of embedded precipitates of SrMoO<sub>4</sub> were quoted only for  $B = 8$  T. A native SrMoO<sub>4</sub> barrier layer was detected by X-ray photoelectron spectroscopy on the surface of SFMO thin films sputtered in a H<sub>2</sub>/Ar atmosphere at 750 °C.<sup>[34]</sup>

Table 1 consists of solely ceramic technologies of composite fabrication. However, thin films of perovskite-spinel composites are known to be manufactured onto SrTiO<sub>3</sub> substrates both by PLD<sup>[157,158]</sup> and by ceramic target magnetron sputtering.<sup>[159]</sup>

The addition of a second phase in composites, which is most likely located at the GBs, improves the barrier for spin-dependent intergranular tunneling. Thereby, the crystal structure of SFMO should not be changed. The original grain boundary is replaced by a nonmagnetic, insulating compound that separates the ferromagnetic half-metallic grains, thereby increasing resistivity. On the other hand, MR decreases rapidly at higher temperatures due to an enhancement of spin-independent electron hopping through localized states induced even by the second phase.

In the case of SFMO-Al composites, contradictory experimental results were reported by the same group nearly at the same time.<sup>[160,161]</sup> A decrement in LFMR values was obtained in ref. [160] attributed to the presence of metallic Ag at the GBs, which suppresses spin-polarized tunneling and, finally reduces magnetoresistance. On the other hand, the enhancement of LFMR was explained in terms of the formation of nonmagnetic patches like Mo-O-Ag-O-Mo-O within the grain, which acts as insulating tunnel barrier.<sup>[161]</sup> For that reason, these data were not considered in Table 1.

LFMR similar to SFMO also occurs in manganites. It is adjusted by forming composites with borosilicate glass,<sup>[162]</sup> CeO<sub>2</sub>,<sup>[163]</sup> Y-stabilized ZrO<sub>2</sub>,<sup>[164]</sup> TiO<sub>2</sub>,<sup>[165]</sup> SrTiO<sub>3</sub>,<sup>[166,167]</sup> SrZrO<sub>3</sub>,<sup>[167]</sup> CoFe<sub>2</sub>O<sub>4</sub>,<sup>[168]</sup> polymers,<sup>[169]</sup> etc., by doping<sup>[170]</sup> or adapting grain size.<sup>[171,172]</sup> However, this occurs only at temperatures much lower than  $T_C$ . MR associated with intergranular transport of spin-polarized electrons is known also in Fe<sub>3</sub>O<sub>4</sub>.<sup>[173]</sup>

Unfortunately, the grain size dependence of LFMR (Figure 6) possesses a minimum just in the region of about 50...100 nm, the typical column size of thin films fabricated by PLD.<sup>[177]</sup> This significantly limits the prospects of LFMR improvement by grain size tuning of thin films.

## 4. Film Deposition Methods

A number of comprehensive books have already been published on the subject of thin film technology,<sup>[178–182]</sup> particularly PLD<sup>[177,183]</sup>. In this section, we consider particular problems of SFMO thin film deposition.

With regard to the peculiarities described in Section 2 and 3, SFMO thin film deposition is a very complex subject involving issues of phase purity, stoichiometry, and Fe/Mo ordering.

The deposition of stoichiometric SFMO has been reported at a high temperature, usually above 800 °C, which is not compatible with silicon technology. SFMO thin films could be formed: 1) by a two-step process comprising the formation of a polymeric film by chemical solution deposition (CSD) or by sputter deposition (SP) of amorphous thin films at low substrate temperatures followed by a subsequent high-temperature annealing procedure, or, 2) by a one-step process at sufficiently high substrate temperatures that enable *in situ* crystallization.

The adjustment of the magnetic properties of SFMO is a complex issue, which is affected by: 1) the choice of the substrate, 2) the limited range of oxygen partial pressure and substrate temperature, and, 3) the postdeposition treatment.

Three particular thin film techniques have been mostly studied for SFMO thin film deposition: PLD, ceramic target magnetron sputtering (MSP), and CSD. Each of these techniques has its own advantages, disadvantages, and manufacturing capabilities. However, the overwhelming majority of studies is devoted to PLD.

### 4.1. Pulsed Laser Deposition

In PLD, a high-energy laser pulse (mostly in the UV range) with very short pulse durations (laser fluence up to a few J cm<sup>-2</sup>) is directed in vacuum or in the presence of a background gas at low pressures onto a small area of a pure, stoichiometric target synthesized by ceramic or sol-gel technology. Target quality is an important issue. Dense nanogrammed targets fabricated by wet chemistry methods are advantageous.<sup>[184,185]</sup> The absorbed laser energy leads to the ablation of atoms, molecules, ions, agglomerates, molten droplets, etc., forming an expanding so-called plasma plume. Due to simultaneous evaporation of all the components in the target, irrespective of their binding energies, the stoichiometry of the material is preserved in the plasma plume. This enables the transfer of target stoichiometry into the thin film.<sup>[182]</sup> Another feature of PLD is its pulsed nature. In between the pulses, film growth is not disturbed by new incident species. Thus, additional surface diffusion occurs, favoring a higher crystallinity and layer-by-layer growth. As a result, PLD is a suitable technique to grow films of complex oxides such as double perovskites. For this reason, the majority of SFMO thin film depositions have been performed by this method.

Film nucleation and growth are driven by the thermal conditions at the substrate. On the other hand, the translational energy of incident species is much higher, in the range of 1–100 eV (10<sup>4</sup>–10<sup>6</sup> K). Substrate temperatures reported for PLD in most of literature are found to be around 950 °C or higher because PLD film growth is dominated by kinetic processes where higher temperatures facilitate atom mobility during deposition. For research purposes, the substrate is placed off-axis at the edge of the plume to restrict the incorporation of agglomerates and droplets into the film. However, this significantly lowers the efficiency of material usage. Moreover, the substrate size is usually in the order of about 1 cm<sup>2</sup>.

There are reports on PLD of complex oxide thin films onto Si wafers with up to 200 mm in diameter.<sup>[186]</sup> However, information about SFMO deposition is still missing and PLD is not mastered yet in real production. Large-area PLD uses laser beam homogenization, beam shaping, and steering. Nevertheless, problems remain due to crater formation on the target as well as cluster and droplet splashing. For example, oxygen-deficient or nonstoichiometric parts of a target created by ablation will be transferred into oxygen-deficient or nonstoichiometric areas in the film, respectively, affecting the physical properties of the entire film.

PLD synthesis of double perovskite oxides requires tuning of the different oxidation behavior of transition metals.<sup>[93]</sup> For the deposition of oxide thin films exhibiting a preselected perovskite phase or a B-site ordering in double perovskites, the main two parameters of the growing film environment, oxygen partial pressure  $p_{O_2}$  and substrate temperature  $T_s$ , are usually adjusted to provide conditions favorable for the formation of the desired film structure.<sup>[145,187–191]</sup> B-site ordering is known to become stable only at a large-enough size and a valence difference of the B' and B'' cations of about 15...20 pm and 2.5...3, respectively.<sup>[192]</sup> PLD favors a kinetically driven spontaneous ordering where the driving force is the difference in ionic radii and the oxidation states of the two B-site cations.<sup>[187–190]</sup> Here, on completion of deposition the films should be quenched to room temperature to freeze the ion positions in the lattice, preserving the achieved cation ordering. In this context, optimum SFMO film growth conditions were related to the crossover point of the thermodynamic  $MoO_3/MoO_2$  and  $Fe_2O_3/Fe_3O_4$  coexistence lines in a  $p_{O_2}-T_s$  phase diagram.<sup>[145]</sup> Generally, the window of growth conditions for highly ordered double-perovskite thin films is very narrow.<sup>[145,187–190]</sup> With regard to the strong effect of ASD on the magnetic properties (cf. Section 3.1), this turns out to be another challenge for the deposition of SFMO thin films suitable for application.

The importance of temperature and partial oxygen pressures to obtain the correct phase of complex oxides is known in the particular case of  $YBa_2Cu_3O_y$  for already 30 years.<sup>[193]</sup> The stability regions of the required oxidation states of the cations can be roughly identified from the thermodynamic  $p_{O_2}-T_s$  phase diagram. A compilation of SFMO thin film deposition by means of PLD is given in Table S3, Supporting Information. Based on these data, a  $p_{O_2}-T_s$  phase diagram was built, revealing the conditions of pure SFMO phase formation by PLD (Figure 7).

PLD is a strongly nonequilibrium process. Ablated species possessing translational energies of 1–100 eV are quenched within a time  $t = a/R$ , where  $a$  is the lattice constant and  $R$  the deposition rate. The incident species do not have enough time to reach an equilibrium configuration before their mobility is lost by interaction with the substrate. The higher the substrate temperature, the greater the surface mobility and the closer the thin film to equilibrium. Ordering of B-site cations Fe and Mo suggests approximate equilibrium conditions at a synthesis temperatures of 1200 °C on a timescale of 50 h.<sup>[70]</sup> Consequently, the optimum growth conditions in Figure 7 are far from equilibrium. They appear at much higher oxygen partial pressures than the ones specified for equilibrium in Section 2.1.

Nonmagnetic  $SrMoO_4$  is a common impurity in polycrystalline SFMO and in SFMO thin films occurring at high

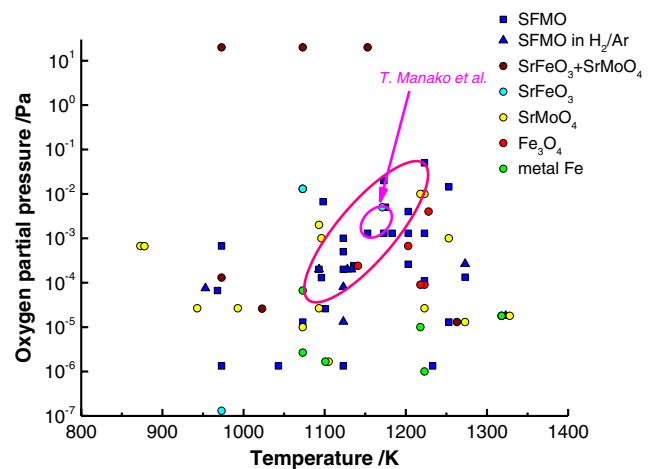


**Figure 7.** Film growth conditions in a  $p_{O_2}-T_s$  plot. Squares, triangles—pure-phase films; circles—impurity phases. Data taken from Supporting Information (Table S3, Supporting Information).

$p_{O_2}$ .<sup>[154,176,194–196]</sup> In particular, it appeared during postdeposition cooling in an oxygen atmosphere.<sup>[197]</sup>  $SrMoO_4$  formation is favored by biaxial tensile film strains.<sup>[110]</sup> During pulse laser deposition of thin films at 820 °C,<sup>[96]</sup> over 850 °C,<sup>[117]</sup> at 900 °C,<sup>[115]</sup> and at 950 °C,<sup>[194,198]</sup> decomposition of SFMO into  $SrMoO_4$  and other oxides was obtained already at  $p_{O_2} > 10^{-2}$  Pa. The appearance of  $SrMoO_4$  causes an increase in film resistivity,<sup>[32,96]</sup> thus strengthening the GB insulating barriers as described in Section 3.3.

Other impurity phases obtained in SFMO are metallic Fe, Fe oxides, and  $SrFeO_{3-\delta}$ . Metallic Fe occurs under too much reducing conditions.<sup>[32,46,117,185,194–196,198,199]</sup> Due to a different nucleation and growth mechanism, their tendency to form epitaxial Fe becomes more pronounced on (111)-oriented films.<sup>[46]</sup> The peaks associated with Fe disappeared from the XRD pattern after postdeposition annealing at 900 °C for 4 h in 5%  $H_2/Ar$  atmosphere and the  $M_s$  value increased from 2.8 to 3.3  $\mu_B/f.u.$  In SFMO thin film deposited onto Si(100) substrates, metallic Fe appears at higher oxygen partial pressures.<sup>[112]</sup>  $Fe_3O_4$  is formed under very oxidizing conditions.<sup>[194,198]</sup>  $SrMoO_4$  coexists with iron oxides<sup>[154]</sup> and iron.<sup>[100]</sup> Also SFMO decomposes into  $SrMoO_4$  and  $SrFeO_{3-\delta}$  at very high oxygen partial pressures.<sup>[153]</sup>  $SrFeO_{3-\delta}$ , as a decomposition product, was obtained in small quantities in SFMO thin films deposited at a higher laser fluence.<sup>[115]</sup> In ref. [118], the impurity phase was attributed to  $SrFe_{1.5}Mo_{0.5}O_{6-\delta}$ . It has to be taken into account that parasitic magnetic phases such as from Fe, iron oxides, and  $SrFeO_{3-\delta}$  increase magnetization. If the presence of such impurities is overlooked, then an overestimation of saturation magnetization attributed to the SFMO phase may occur.<sup>[98]</sup>

With regard to Section 2.6 and 3.3, the most popular substrate for growing  $Sr_2FeMoO_6$  films is  $SrTiO_3(001)$  due to the close lattice matching between the two materials. Other substrates include  $LaAlO_3(001)$ ,  $MgO(001)$ ,  $NdGaO_3(001)$  ( $(LaAlO_3)_{0.3}(Sr_2AlTaO_6)_{0.7}(001)$  (LSAT),  $Sr_2Al_0.3Ga_0.7TaO_6(001)$  (SAGT),  $SrLaAlO_4(001)$  (SLAO),  $TbScO_3(110)$  (TSO),  $DyScO_3(110)$  (DSO), and sapphire [Table S3, Supporting Information]. Si(100) substrates were applied with an ultrathin  $SrTiO_3$  buffer layer.<sup>[22]</sup> Only one report used pure Si(100) as substrate.<sup>[112]</sup>

To reduce lattice mismatch, SrTiO<sub>3</sub>(001) substrates were covered with PLD Ba<sub>0.4</sub>Sr<sub>0.6</sub>TiO<sub>3</sub>(001)<sup>[143]</sup> or with spark plasma-sintered polycrystalline Sr<sub>2</sub>MgWO<sub>6</sub>.<sup>[197]</sup> The study in ref. [200] is devoted solely to buffer layer deposition by PLD on SrTiO<sub>3</sub>(001) substrates.

Early work did not find differences in transport and magnetic properties between samples deposited onto SrTiO<sub>3</sub>(001) and LaAlO<sub>3</sub>(001) substrates.<sup>[142]</sup> Later, magnetic and transport properties were shown to be different with smaller magnetic moments for larger lattice mismatch (**Figure 8**). Only data providing lattice constants measured in-plane were taken into account. For comparison, also data for ceramic target sputtering are shown.

## 4.2. Ceramic Target Sputtering

Sputter deposition or sputtering is a technique in which material species from a so-called target are ejected from its surface by bombardment with high-energetic species originating from the plasma. In thin film deposition technology, low-pressure plasmas are ignited between the target and the substrate, mostly in an Ar atmosphere providing Ar<sup>+</sup> ions for this purpose. The operational pressure defines the mean free path of Ar<sup>+</sup> ions and the sputtered species. If the mean free path is smaller than the target–substrate distance, then cluster formation becomes possible. At too low pressure, the degree of thermalization of the sputtered species is low, and a surface bombardment with energetic particles results. It is optimal when there are just a few collisions in the target–substrate gap. For a direct synthesis of oxides, nitrides, etc., reactive sputtering is applied. Here, gases such as oxygen or nitrogen, in addition to Ar, are introduced into the chamber during film growth. The plasma may be driven by DC, pulsed DC, and RF generators. DC sputtering suffers from charge buildup at insulating surfaces. This surface charge develops a significant voltage drop across insulating layers. Electrical breakdown of the insulating layer then initiates arcing. This

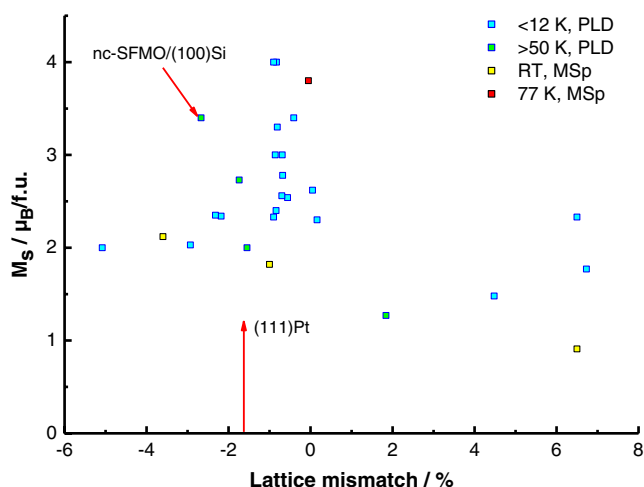


**Figure 8.** Saturation magnetization as a function of lattice mismatch for PLD (data from refs. [S9, S12, S22, S25, S29, S36, S42, S44, S47], Table S3, Supporting Information) and for ceramic target magnetron sputtering (MSp) (data from refs. [S49, S52, S58], Table S4, Supporting Information).

deteriorates film quality due to crater formation at the target surface and the splashing of droplets and agglomerates. To prevent surface charge buildup, RF (mostly at 13.56 MHz) sources are used. Pulsed DC is a periodically interrupted DC with similar behavior to an RF source.

A magnetron sputtering source takes advantage of the confinement of the low-pressure plasma to a region close to the target. Electrons are held by a magnetic field exhibiting increasing strength in all planar directions in a cycloidal path near the target long enough to greatly increase the number colliding with the background gas. This leads to a higher plasma density and increased deposition rates.

Since sputtering does not require melting or evaporation of the source material, nearly all materials can be deposited by magnetron sputtering, regardless of their melting temperature. Film texture is determined by the ratio of the substrate temperature to the melting temperature of the source material and the energy flux carried from the plasma to the growing surface.<sup>[201]</sup> At temperatures suitable for silicon technology, sputtered thin films exhibit a columnar texture, e.g., these films will be in an intermediate state between tetragonal 4 mm symmetry of single crystals and oom symmetry of ceramics. Consequently, the interpretation of grain size parameter will be very different from bulk ceramics.

A compilation of SFMO thin film deposition by means of sputter techniques is given in Table S4, Supporting Information. Film deposition is performed either by ceramic target MSP or by argon ion beam sputtering (IBSP) in a narrow technology window of  $T_s = 750\text{--}950\text{ }^\circ\text{C}$  and  $p_{O_2} \approx 4 \times 10^{-6}\text{--}3 \times 10^{-5}\text{ Pa}$ . The optimal  $p_{O_2}$  values are about one order of magnitude lower than for PLD since sputtering is closer to thermal equilibrium. To provide low-enough oxygen partial pressures, the majority of reports use a H<sub>2</sub>/Ar gas atmosphere.

Ceramic target MSP of multicomponent oxides suffers from different sputter yields of the individual components. Generally, sputter yield depends on atomic masses and the surface binding energies of the different components present in the target. Lighter elements are preferentially sputtered. For similar masses, the surface binding energy determines the sputter yield. In the case of SFMO, the masses of Sr and Mo are close to each other, while Fe has a lighter one. Then again, the dissociation energies of the metal–oxygen bond are not very different ranging from 4.4 eV for Fe up to 5.2 eV for Mo.<sup>[202]</sup> The listed peculiarities require a long pre-sputtering step until a steady state at the target surface is reached. Since atom scattering in the gas phase is also mass-dependent (lighter atoms scatter more widely), a desired composition will be transferred to the film only in a very narrow range of operational pressures allocating the mean free path of sputtering atoms. The same problems arise for IBSP. Here, the kinetic energy of Ar<sup>+</sup> ions impinging at the target can be controlled separately. It is mostly higher than for MSP, providing higher sputter yields. However, the sputtered target area is usually small.

Substrates used for SFMO sputter deposition are SrTiO<sub>3</sub>(001), LaAlO<sub>3</sub>(001), MgO(001), polycrystalline Ba<sub>0.5</sub>Sr<sub>0.5</sub>TiO<sub>3</sub>, and sapphire ceramics. To improve lattice mismatch, SrTiO<sub>3</sub>(001) substrates were covered with Ba<sub>0.4</sub>Sr<sub>0.6</sub>TiO<sub>3</sub>(001),<sup>[104]</sup> Sr<sub>2</sub>GaTaO<sub>6</sub>(001), and Sr<sub>2</sub>CrNbO<sub>6</sub>(001),<sup>[203]</sup> as well as LSAT substrates with Sr<sub>2</sub>CrNbO<sub>6</sub>(001) buffer layers.<sup>[203]</sup> In particular, Ba<sub>0.4</sub>Sr<sub>0.6</sub>TiO<sub>3</sub> was selected as a buffer layer since its bulk lattice constant

( $2 \times 0.3948 = 0.7896$  nm) almost completely matches with the one of bulk SFMO (0.7892 nm). The  $\text{Ba}_{0.4}\text{Sr}_{0.6}\text{TiO}_3$  buffer layer was shown to improve also B-site ordering, lowering the ASD of (111)-oriented thin films deposited from 0.135 for films on a bare  $\text{SrTiO}_3(111)$  substrate to 0.05 for films on a  $\text{SrTiO}_3(111)$  substrate with a lattice-matched  $\text{Ba}_{0.4}\text{Sr}_{0.6}\text{TiO}_3$  buffer layer.<sup>[34]</sup> The role of lattice mismatch on B-site ordering was emphasized also in ref. [204]. Similar to PLD films (cf. Figure 8), saturation magnetization  $M_s$  reduces as the magnitude of lattice mismatch between SFMO and the substrate worsens. This was assigned to the formation of a so-called dead layer near the substrate–film interface. With thickness decreasing up to 30 nm, films on  $\text{Ba}_{0.5}\text{Sr}_{0.5}\text{TiO}_3$  showed an initial rise of MR value at 22 K and then a dip for the 15-nm-thick film. Such an extrinsic behavior was associated with peculiarities of grain orientation induced by the polycrystalline substrate.

Off-axis sputtering is a suitable research method providing epitaxial growth and improved crystallinity.<sup>[116]</sup> Here, the substrate is oriented perpendicularly to the surface of the target and replaced away from the center. This avoids bombardment by high-energy particles. However, in the considered case, material utilization and the substrate size ( $5 \times 5$  mm<sup>2</sup>) were small. Phase-pure and highly ordered ( $S = 0.854$ ) SFMO films were fabricated on  $\text{SrTiO}_3(111)$  substrates by carefully controlling Fe/Mo stoichiometry and by optimizing background gas and gas pressure. Films deposited onto  $\text{SrTiO}_3(001)$  substrates were less ordered and had a slightly higher out-of-plane lattice constant. The trend that smaller lattice constants are related to better film properties was found to be a general behavior in sputtered SFMO thin films.<sup>[205]</sup>

Several impurity phases have been detected in sputtered SFMO films:  $\text{SrMoO}_4$  and iron oxides formed under very oxidizing conditions in films on  $\text{LaAlO}_3(111)$ <sup>[116,204]</sup> as well as  $\text{SrMoO}_4$  and  $\text{SrFeO}_{3-\delta}$  in films deposited by IBSP onto corundum ceramics substrates at deposition rates of 1.8 and 0.7 nm min<sup>-1</sup>, respectively.<sup>[206]</sup> In the first case, the appearance of impurity phases depends on the kind of the substrate and thickness.<sup>[204]</sup> SFMO films on  $\text{SrTiO}_3(001)$  substrates included an additional SrO phase created by  $\text{SrTiO}_3$  decomposition at 950 °C. Very thin films (30 nm) on  $\text{MgO}(001)$  and  $\text{LaAlO}_3(001)$  substrates were Fe-rich with compositions of  $\text{Sr}_{1.75}\text{Fe}_{1.35}\text{Mo}_{0.91}\text{O}_{6+\delta}$  and of  $\text{Sr}_{1.89}\text{Fe}_{1.23}\text{Mo}_{0.89}\text{O}_{6+\delta}$ , respectively. The larger Fe content occurring in the thin layer gives evidence of a Fe-rich layer at the substrate–film interface layer. For a film thickness of 240 nm, the dependence of composition on substrate type disappeared. Polycrystalline  $\text{Sr}_{0.5}\text{Ba}_{0.5}\text{TiO}_3$  revealed a more complex behavior. It possesses many XRD peaks caused by the polycrystalline nature of the substrate. Here, apart from iron oxide and  $\text{SrMoO}_4$ ,  $\text{SrFeO}_{3-\delta}$  also became visible. According to ref. [116], the Mo content of SFMO films increases monotonically with increasing Ar pressure in the chamber. At higher pressures, this favors the formation of the  $\text{SrMoO}_4$  impurity phase. Supposing a constant residual oxygen content, the cited increase of the Ar pressure means simultaneously an increase of oxygen partial pressure by more than an order of magnitude. On the other hand,  $p_{\text{O}_2}$  buildup in the chamber originating from sputtered oxygen also increases at higher pressures.

Surprisingly, reports on a direct synthesis of SFMO thin films by reactive sputtering are still missing. One reason might be that

all used target materials are easily oxidizing,<sup>[202]</sup> that is, their behavior will be similar to a Pb target in  $\text{PbZr}_x\text{Ti}_{1-x}\text{O}_3$  film deposition,<sup>[207]</sup> which does not show any pronounced hysteresis of the spectral intensity of Pb emission from the low-pressure plasma when changing oxygen flow. For increasing and decreasing oxygen flow, the data points coincide, meaning that there is no transition from the metal mode to the oxide mode of sputtering. The target surface is always poisoned by a thin oxide layer. That always causes that oxide to sputter with a typical low sputter yield. Another reason is that in a multitarget system, adjusting the type of power supply to each target—the power supplied to the target, individual oxygen flow, operational pressure, etc.—is very cumbersome.

### 4.3. Chemical Solution Deposition

CSD is a non-vacuum, wet chemical technique of preparing a chemical solution from precursor chemicals and depositing it onto a substrate by means of available methodologies (spin coating, dip coating, web coating, ink jet printing, etc.). CSD ranges from the sol-gel process to metal-organic decomposition (MOD). In the sol-gel process, a controlled initial hydrolysis stage occurs, allowing the condensation reaction to proceed leading to the formation of a polymer network. MOD consists of a process where metal-organic precursors decompose to produce the required film. Further multistage heat treatments cause further pyrolysis, drying, carbon removal, nucleation of crystallites, and final crystallization. Here, crystallization is accompanied by a large volume change, creating film strain.

CSD is suitable for the fabrication of multicomponent thin films such as SFMO since it enables a precise composition control that provides high purity and a good film homogeneity, and all at comparably lower costs.

SFMO film deposition makes use of a variety of heat treatment procedures<sup>[208–210]</sup>: 1) drying and  $\text{SrMoO}_4$  precursor formation at 300–400 °C, 2) calcination in oxygen-containing atmosphere to remove carbon and creating a mixture of  $\text{SrMoO}_4$  and  $\text{SrFeO}_{3-\delta}$  at 700–750 °C, and 3) reduction of  $\text{SrMoO}_4$  and Fe/Mo ordering at 850–900 °C.

Available results of SFMO CSD are compiled in Table S5, Supporting Information. Sufficient B-site ordering was obtained only for a special procedure of solution manufacturing, including a separate preparation of  $(\text{Sr}(\text{O}^i\text{Pr})_2(\text{Fe}(\text{acac})_3)_-$  and  $(\text{MoO}_2(\text{acac})_2)_-$  solutions in 1-PrOH/2 and mixing them after 12 h hydrolysis. On the other hand, there is a large body of SFMO powder fabrication with different kinds of wet chemistry methods, including nanoscaled material (cf., for instance<sup>[184]</sup>). Here, SFMO is usually crystallized at temperatures exceeding 1000 °C, that is, much above the temperature of  $\text{SrTiO}_3$  substrate stability.<sup>[211]</sup>

### 4.4. Other Methods

SFMO and  $\text{Sr}_3\text{FeMoO}_7$  thin films were fabricated by spray pyrolysis in ref. [212]. A solution of Sr and Fe chlorides as well as ammonium molybdate-tetrahydrate was sprayed onto a heated silica glass substrate. SFMO was formed at 460 °C;  $\text{Sr}_3\text{FeMoO}_7$  at 480 °C. Optical and thermal properties were investigated, but

no magnetic properties were reported. The obtained optical gaps of  $2.31 \pm 0.08$  and  $2.28 \pm 0.08$  eV of SFMO and  $\text{Sr}_3\text{FeMoO}_7$ , respectively, are characteristic for wide-bandgap semiconductors.

SFMO thin films have been prepared via ultrasonic spray pyrolysis on  $\text{LaAlO}_3(001)$  substrates at temperatures between 600 and 900 °C followed by postannealing at 1200 °C in 5%  $\text{H}_2/\text{Ar}$  for 5 h.<sup>[213]</sup> This method does not require vacuum conditions. A mist is generated from an aqueous solution containing dissolved Sr and Fe nitrates and ammonia-complexed molybdic acid by means of vibrations of ultrasonic transducers. Argon is used as a carrier gas to transfer the mist onto the heated substrate where pyrolysis occurs. The deposition rate amounted to  $\approx 10 \text{ nm min}^{-1}$ .  $\text{SrMoO}_4$  present in the as-deposited films disappears after annealing, thereby acting as a seed for SFMO growth. Only films deposited at 900 °C showed metallic conductivity. The  $M_s$  value at 4.2 K was  $\approx 2.5 \mu_B/\text{f.u.}$ , the MR values at 1 T were  $-0.24\%$  and  $< -0.05\%$  at 50 K and room temperature, respectively. The MR effect at 1 T increases in less ordered films with decreasing substrate temperature up to  $\approx -2.3\%$  for films deposited at 600 °C. The films possess a spin polarization of  $\approx 60\% \pm 3\%$  as measured by the Andreev point contact technique, independent on the film deposition temperature.

In electrophoretic deposition, colloidal particles suspended in a liquid acquire an electric charge and migrate in an electric field to one of the electrodes, forming a coherent deposit. This deposit is then subjected to further thermal treatment. Electrophoretic deposition of SFMO layers was reported in ref. [214]. Finely ground SFMO powder in a  $\text{I}_2$ -acetone mixture was sedimented onto single-crystalline Si substrates exhibiting a resistivity of about  $2.8 \text{ m}\Omega \text{ m}$ . The postannealing treatment was performed at 900...1100 °C in a 5%  $\text{H}_2/\text{Ar}$  atmosphere. The single-phase layers formed at an annealing temperature of 1100 °C showed a ferromagnetic-paramagnetic phase transition with  $T_C = 282 \text{ K}$ , which is lower than that of the parent powder.  $\text{SrMoO}_4$  appeared in layers annealed at lower temperatures, decreasing the  $T_C$  value further. In another report,<sup>[215]</sup> SFMO powders were manufactured by means of the citrate-gel method. Ethanol with 0.1 vol% phosphate ester as well as isopropyl alcohol with 2 vol%  $\text{I}_2$ -acetone were used for suspension preparation since the SFMO particles in an aqueous solution under ultrasonic treatment completely decomposed into  $\text{Fe}_2\text{O}_3$ ,  $\text{SrMoO}_4$ , and  $\text{SrCO}_3$  phases. Stainless steel plates were used as conducting substrates. Deposits obtained in pure ethanol were highly agglomerated and nonuniform. No postdeposition treatment was communicated. Layers sedimented from the ethanol-phosphate ester mixture were more uniform and had a higher density compared with that from the isopropyl alcohol-( $\text{I}_2$ -acetone) mixture. The coexistence of  $\text{Fe}^{3+}\text{-Mo}^{5+}$  and  $\text{Fe}^{2+}\text{-Mo}^{6+}$  pairs was proved by X-ray photoelectron spectroscopy.

SFMO thick films possessing an ASD  $\approx 0.12$  were screen-printed by mixing calcined SFMO powder with a terpeneol binder and annealing the printed film in three steps up to 1400 °C under flowing oxygen.<sup>[35]</sup> Due to the granular structure of the films, they degrade quickly at room temperature forming  $\text{SrMoO}_4$  at GBs.

In molecular beam epitaxy (MBE), several atomic or molecular beams from evaporation sources are directed to the substrate in ultra-high vacuum conditions ( $p < 10^{-8} \text{ Pa}$ ). This allows the growth of very high-quality thin films of low defect density.

However, the strongly reducing conditions of MBE are detrimental to SFMO deposition.

Metal-organic chemical vapor deposition provides film growth via chemical reaction at elevated temperatures and reduces pressure, creating high-purity thin films. SFMO deposition suffers from the absence of suitable Fe sources.  $\text{Fe}(\text{THMD})_3$  is hygroscopic, has a melting point of 180 °C, and decomposes above 300 °C.<sup>[216]</sup> An alternative is  $\text{Fe}(\text{TBOB})_3$  that possesses sublimation temperatures between 350 and 500 °C at 270 Pa.<sup>[217]</sup>

## 5. Conclusions

Strontium ferromolybdate is a promising material for magnetic field sensors due to its excellent magnetic properties: i) saturation magnetization of  $4 \mu_B/\text{f.u.}$ ; ii) high spin polarization up to 100%; iii) high Curie temperature up to 420 K; and iv) presence of a low-field magnetoresistance. However, the experimental values of saturation magnetization, spin polarization, and Curie temperature have been reported to be significantly lower in most studies. Also, achieving these value in thin-film materials appears to be challenging.

The magnetic properties of SFMO are very sensitive to B-site disorder and deviations from cation and oxygen stoichiometry. This requires a precise composition control during film manufacturing. Although PLD provides a stoichiometric transfer of the target composition into the thin film, it is not suitable for large-scale device fabrication. Large-area deposition by ceramic target sputtering suffers from transferring the target composition adequately into the film. Attempts of CSD did not provide highly ordered films. Thus, a direct synthesis by reactive multitarget sputtering comes into the focus as a promising approach for industrial device fabrication. Here, the handling of three easily oxidizing metal targets requires a sophisticated target power supply and a precise control of deposition conditions.

Reasonable costs of SFMO-based MTJ thin-film devices require a silicon substrate-based fabrication technology. This limits significantly the acceptable substrate temperatures, thereby deteriorating B-site order. A proper solution to this problem needs further research on additional nonthermal stimulations of growth processes on film surface. An approach to increase the surface temperature of the substrate is the use of energy that a low-pressure plasma carries to the substrate surface. By this way, the effective substrate temperature could be increased by about 200...300 °C.<sup>[218,219]</sup>

Another concept of SFMO MTJ devices is the use of nanosized core-shell particles where the shell acts as a tunnel barrier. However, this concept is beyond the scope of this work.

## Supporting Information

Supporting Information is available from the Wiley Online Library or from the author.

## Acknowledgements

The work was supported by the European project H2020-MSCA-RISE-2017-778308-SPINMULTIFILM.

## Conflict of Interest

The authors declare no conflict of interest.

## Keywords

magnetic properties, point defects, stoichiometry, strontium ferromolybdate, thin films

Received: June 2, 2019

Revised: August 11, 2019

Published online:

- [1] G. H. Jonker, J. H. Van Santen, *Physica* **1950**, 16, 337.
- [2] K.-I. Kobayashi, T. Kimura, H. Sawada, K. Terakura, Y. Tokura, *Nature* **1998**, 395, 677.
- [3] K. Panetta, *5 Trends Emerge in the Gartner Hype Cycle for Emerging Technologies*, <https://www.gartner.com/smarterwithgartner/5-trends-emerge-in-gartner-hype-cycle-for-emerging-technologies-2018/>, **2018** (accessed: August 2019).
- [4] K. Momma, F. Izumi, *J. Appl. Crystallogr.* **2011**, 44, 1272.
- [5] W. A. Adeagbo, M. Hoffmann, A. Ernst, W. Hergert, M. Saloaro, P. Paturi, K. Kokko, *Phys. Rev. Mater.* **2018**, 2, 083604.
- [6] R. Mishra, O. D. Restrepo, P. M. Woodward, W. Windl, *Chem. Mater.* **2010**, 22, 6092.
- [7] Y. Zhang, V. Ji, K.-W. Xu, *J. Alloys Compd.* **2015**, 648, 374.
- [8] A. S. Ogale, S. B. Ogale, R. Ramesh, T. Venkatesan, *Appl. Phys. Lett.* **1999**, 75, 537.
- [9] T. Saha-Dasgupta, D. D. Sarma, *Phys. Rev. B* **2001**, 64, 064408.
- [10] I. V. Solov'yev, *Phys. Rev. B* **2002**, 65, 144446.
- [11] D. Stoeffler, S. Colis, *J. Phys.: Condens. Matter* **2005**, 17, 6415.
- [12] L. Harnagea, P. Berthet, *J. Solid State Chem.* **2015**, 222, 115.
- [13] M. Saloaro, M. Hoffmann, W. A. Adeagbo, S. Granroth, H. Deniz, H. Palonen, H. Huhtinen, S. Majumdar, P. Laukkanen, W. Hergert, A. Ernst, P. Paturi, *ACS Appl. Mater. Interfaces* **2016**, 8, 20440.
- [14] A. B. Muñoz-García, M. Pavone, E. A. Carter, *Chem. Mater.* **2011**, 23, 4525.
- [15] H. Wu, Y. Ma, Y. Qian, E. Kan, R. Lu, Y. Liu, W. Tan, C. Xiao, K. Deng, *Solid State Commun.* **2014**, 177, 57.
- [16] M. Lü, J. Li, X. Hao, Z. Yang, D. Zhou, J. Meng, *J. Phys.: Condens. Matter* **2008**, 20, 175213.
- [17] Y. Moritomo, N. Shimamoto, S. Xu, A. Machida, E. Nishibori, M. Takata, M. Sakata, A. Nakamura, *Jpn. J. Appl. Phys.* **2001**, 40, L672.
- [18] S. A. Wolf, D. D. Awschalom, R. A. Buhrman, J. M. Daughton, S. von Molnár, M. L. Roukes, A. Y. Chtchelkanova, D. M. Treger, *Science* **2001**, 294, 1488.
- [19] M. Tondra, J. M. Daughton, D. Wang, R. S. Beech, A. Fink, J. A. Taylor, *J. Appl. Phys.* **1998**, 83, 6688.
- [20] W. H. Butler, X.-G. Zhang, T. C. Schulthess, J. M. MacLaren, *Phys. Rev. B* **2001**, 63, 054416.
- [21] J. Mathon, A. Umerski, *Phys. Rev. B* **2001**, 63, 220403.
- [22] N. Kumar, P. Misra, R. K. Kotla, A. Gaur, R. S. Katiyar, *J. Phys. D: Appl. Phys.* **2014**, 47, 065006.
- [23] P. Majewski, J. Rager, C. Schurr, F. Aldinger, *Int. J. Inorg. Mater.* **2001**, 3, 733.
- [24] J. Rager, M. Zipperle, A. Sharma, J. L. MacManus-Driscoll, *J. Am. Ceram. Soc.* **2004**, 87, 1330.
- [25] B. García-Landa, C. Ritter, M. R. Ibarra, J. Blasco, P. A. Algarabel, R. Mahendiran, J. García, *Solid State Commun.* **1999**, 110, 435.
- [26] J. Töpfer, R. Kircheisen, S. Barth, *J. Appl. Phys.* **2009**, 105, 07D712.
- [27] R. Kircheisen, J. Töpfer, *J. Solid State Chem.* **2012**, 185, 76.
- [28] T. Nakamura, K. Kuniyama, Y. Hirose, *Mater. Res. Bull.* **1981**, 16, 321.
- [29] A. Sharma, J. L. MacManus-Driscoll, W. Branford, Y. Bugoslavsky, L. F. Cohen, J. Rager, *Appl. Phys. Lett.* **2005**, 87, 112505.
- [30] T.-T. Fang, T.-F. Ko, *J. Am. Ceram. Soc.* **2003**, 86, 1453.
- [31] D. Niebieskikwiat, R. D. Sanchez, A. Caneiro, L. Morales, M. Vásquez-Mansilla, F. Rivadulla, L. E. Hueso, *Phys. Rev. B* **2000**, 62, 3340.
- [32] S. R. Shinde, S. B. Ogale, R. L. Greene, T. Venkatesan, K. Tsoi, S. W. Cheong, A. J. Millis, *J. Appl. Phys.* **2003**, 93, 1605.
- [33] T. Ishigaki, S. Yamauchi, K. Kishio, J. Mizusaki, K. Fueki, *J. Solid State Chem.* **1988**, 73, 179.
- [34] N. Koduka, Y. Takahashi, K. Imaeda, H. Asano, M. Matsui, *J. Magn. Soc. Jpn.* **2006**, 30, 374.
- [35] J. Navarro, C. Frontera, D. Rubi, N. Mestres, J. Fontcuberta, *Mater. Res. Bull.* **2003**, 38, 1477.
- [36] L. H. Son, N. X. Phuc, P. V. Phuc, N. M. Hong, L. V. Hong, *J. Raman Spectrosc.* **2001**, 32, 817.
- [37] K. Kuepper, M. Raekers, C. Taubitz, H. Hesse, M. Neumann, A. T. Young, C. Piamonteze, F. Bondino, K. C. Prince, *J. Appl. Phys.* **2008**, 104, 036103.
- [38] D. Sánchez, J. A. Alonso, M. García-Hernández, M. J. Martínez-Lope, M. T. Casais, J. L. Martínez, M. T. Fernández-Díaz, *J. Magn. Mater.* **2004**, 272–276, 1732.
- [39] S. R. Popuri, D. Redpath, G. Chan, R. I. Smith, O. Cespedes, J.-W. G. Bos, *Dalton Trans.* **2015**, 23, 10621.
- [40] F. Sher, A. J. Williams, A. Venimadhav, M. G. Blamire, J. P. Attfield, *Chem. Mater.* **2005**, 17, 1792.
- [41] J. H. Haeni, C. D. Theis, D. G. Schlom, W. Tian, X. Q. Pan, H. Chang, I. Takeuchi, X.-D. Xiang, *Appl. Phys. Lett.* **2001**, 78, 3292.
- [42] G. C. Mather, F. M. Figueiredo, J. Romero de Paz, S. García-Martín, *Inorg. Chem.* **2008**, 47, 921.
- [43] D. J. Gallon, P. D. Battle, S. J. Blundell, J. C. Burley, A. I. Coldea, E. J. Cussen, M. J. Rosseinsky, C. Steer, *Chem. Mater.* **2002**, 14, 3976.
- [44] G. M. Veith, I. D. Fawcett, M. Greenblatt, M. Croft, I. Nowik, *Int. J. Inorg. Mater.* **2000**, 2, 513.
- [45] G. M. Veith, R. Chen, G. Popov, M. Croft, Y. Shokh, I. Nowik, M. Greenblatt, *J. Solid State Chem.* **2002**, 166, 292.
- [46] T. L. Meyer, M. Dixit, R. E. A. Williams, M. A. Susner, H. L. Fraser, D. W. McComb, M. D. Sumption, T. R. Lemberger, P. M. Woodward, *J. Appl. Phys.* **2014**, 116, 013905.
- [47] T. Chakraborty, C. Meneghini, A. Nag, S. Ray, *J. Mater. Chem. C* **2015**, 3, 8127.
- [48] G. M. Veith, M. Greenblatt, M. Croft, K. V. Ramanujachary, J. Hattrick-Simpers, S. E. Lofland, I. Nowik, *Chem. Mater.* **2005**, 17, 2562.
- [49] Z. Li, G. Li, J. Sun, L. You, C.-K. Loong, Y. Wang, F. Liao, J. Lin, *J. Solid State Chem.* **2005**, 178, 3315.
- [50] L. W. Whaley, M. V. Lobanov, D. Sheptyakov, M. Croft, K. V. Ramanujachary, S. Lofland, P. W. Stephens, J.-H. Her, G. Van Tendeloo, M. Rossell, M. Greenblatt, *Chem. Mater.* **2006**, 18, 3448.
- [51] M. Lehtimäki, H. Yamauchi, M. Karppinen, *J. Solid State Chem.* **2013**, 204, 95.
- [52] G. Y. Liu, G. H. Rao, X. M. Feng, H. F. Yang, Z. W. Ouyang, W. F. Liu, J. K. Liang, *J. Phys.: Condens. Matter* **2003**, 15, 2053.
- [53] D. Topwal, D. D. Sarma, H. Kato, Y. Tokura, M. Avignon, *Phys. Rev. B* **2006**, 73, 094419.
- [54] J. R. Suarez, F. Estrada, O. Navarro, M. Avignon, *Eur. Phys. J. B* **2011**, 84, 53.
- [55] K. Yoshida, S. Ikeuchi, H. Shimizu, S. Okayasu, T. Suzuki, *J. Phys. Soc. Jpn.* **2011**, 80, 044716.
- [56] Y. Markandeya, K. Suresh, G. Bhikshamaiah, *J. Alloys Compd.* **2011**, 509, 9598.
- [57] J. R. Hayes, A. P. Grosvenor, *J. Alloys Compd.* **2012**, 537, 323.

- [58] O. Erten, O. Nganba Meetei, A. Mukherjee, M. Randeria, N. Trivedi, P. Woodward, *Phys. Rev. B* **2013**, *87*, 165105.
- [59] W. Ji, J. F. Wang, J. Xu, L. Jiao, J. Zhou, Y. B. Chen, Z. B. Gu, S. H. Yao, S. T. Zhang, Y. F. Chen, *J. Phys. D: Appl. Phys.* **2013**, *46*, 015001.
- [60] N. Kumar, A. Gaur, R. K. Kotnala, *J. Alloys Compd.* **2014**, *601*, 245.
- [61] C. Zener, *Phys. Rev.* **1951**, *82*, 403.
- [62] D. Rubi, J. Navarro, J. Fontcuberta, M. Izquierdo, J. Avila, M. C. Asensio, *J. Phys. Chem. Solids* **2006**, *67*, 575.
- [63] K. Kuepper, I. Balasz, H. Hesse, A. Winiarski, K. C. Prince, M. Matteucci, D. Wett, R. Szargan, E. Burzo, M. Neumann, *Phys. Status Solidi A* **2004**, *201*, 3252.
- [64] M. Besse, V. Cros, A. Barthélémy, H. Jaffrès, J. Vogel, F. Petroff, A. Mirone, A. Tagliaferri, P. Bencok, P. Decorse, P. Berthet, Z. Szotek, W. M. Temmerman, S. S. Dhesi, N. B. Brookes, A. Rogalev, A. Fert, *EPL* **2002**, *60*, 608.
- [65] K. Weiser, *J. Chem. Phys.* **1958**, *7*, 118.
- [66] R. D. Shannon, *Acta Cryst. A* **1976**, *32*, 751.
- [67] V. M. Goldschmidt, *Naturwissenschaften* **1926**, *21*, 477.
- [68] A. Navrotsky, in *Proc. of the 2000 Aspen Winter Conf. on Fundamental Physics of Ferroelectrics*, AIP Conf. Proc. 535, AIP, New York **2000**, pp. 288–296.
- [69] D. Serrate, J. M. De Teresa, M. R. Ibarra, *J. Phys.: Condens. Matter* **2007**, *19*, 023201.
- [70] T. Shimada, J. Nakamura, T. Motohashi, H. Yamauchi, M. Karppinen, *Chem. Mater.* **2003**, *15*, 4494.
- [71] J. H. Song, B.-G. Park, J.-H. Park, Y. H. Jeong, *J. Korean Phys. Soc.* **2008**, *53*, 1084.
- [72] Ll. Balcells, J. Navarro, M. Bibes, A. Roig, B. Martínez, J. Fontcuberta, *Appl. Phys. Lett.* **2001**, *78*, 781.
- [73] B. J. Park, H. Han, J. Kim, Y. J. Kim, C. S. Kim, B. W. Lee, *J. Magn. Magn. Mater.* **2004**, *272–276*, 1851.
- [74] T. Yamamoto, J. Liimatainen, J. Lindén, M. Karppinen, H. Yamauchi, *J. Mater. Chem.* **2000**, *10*, 2342.
- [75] S. Colis, D. Stoeffler, C. Meny, T. Fix, C. Leuvrey, G. Pourroy, A. Dinia, P. J. Panissod, *J. Appl. Phys.* **2005**, *98*, 033905.
- [76] Q. Zhang, Z. F. Xu, L. F. Wang, S. H. Gao, S. J. Yuan, *J. Alloys Compd.* **2015**, *649*, 1151.
- [77] N. Kalanda, V. Turchenko, D. Karpinsky, S. Demyanov, M. Yarmolich, M. Balasoiu, N. Lupu, S. Tyutyunnikov, N. A. Sobolev, *Phys. Status Solidi B* **2018**, *1800278*.
- [78] Y. Yasukawa, J. Lindén, T. S. Chan, R. S. Liu, H. Yamauchi, M. Karppinen, *J. Solid State Chem.* **2004**, *177*, 2655.
- [79] C. Cazorla, *Phys. Rev. Appl.* **2017**, *7*, 044025.
- [80] Y.-L. Lee, D. Morgan, *Phys. Chem. Chem. Phys.* **2012**, *14*, 290.
- [81] A. B. Muñoz-García, A. M. Ritzmann, M. Pavone, J. A. Keith, E. A. Carter, *Acc. Chem. Res.* **2014**, *47*, 3340.
- [82] K. Reuter, M. Scheffler, *Phys. Rev. B* **2001**, *65*, 035406.
- [83] H. Wu, Y. Ma, Y. Qian, E. Kan, R. Lu, Y. Liu, W. Tan, C. Xiao, K. Deng, *Solid State Commun.* **2014**, *177*, 57.
- [84] N. J. Mosey, E. A. Carter, *Phys. Rev. B* **2007**, *76*, 155123.
- [85] C. Freysoldt, B. Grabowski, T. Hickel, J. Neugebauer, G. Kresse, A. Janotti, C. G. Van de Walle, *Rev. Mod. Phys.* **2014**, *86*, 253.
- [86] T. Das, J. D. Nicholas, Y. Qi, *Mater. Chem. A* **2017**, *5*, 4493.
- [87] N. A. Kalanda, *Mod. Electron. Mater.* **2018**, *4*, 1.
- [88] N. Grunbaum, L. Mogni, F. Prado, A. Caneiro, *J. Solid State Chem.* **2004**, *177*, 2350.
- [89] L. Wang, R. Merkle, G. Cristiani, B. Stuhlhofer, H.-U. Haberman, J. Maier, *ECS Trans.* **2008**, *13*, 85.
- [90] R. P. Panguluri, S. Xu, Y. Moritomo, I. V. Solov'yev, B. Nadgorny, *Appl. Phys. Lett.* **2009**, *94*, 012501.
- [91] Y. Tomioka, T. Okuda, Y. Okimoto, R. Kumai, K. I. Kobayashi, *Phys. Rev. B* **2000**, *61*, 422.
- [92] J.-F. Wang, X.-J. Xu, W.-J. Ji, S.-T. Zhang, J. Zhou, Z.-B. Gu, Y. B. Chen, G.-L. Yuan, S.-H. Yao, Y.-F. Chen, *Cryst. Eng. Comm.* **2013**, *15*, 4601.
- [93] E. A. Carter, W. A. Goddard III, *J. Phys. Chem.* **1988**, *92*, 2109.
- [94] D. Niebieskikwiat, A. Caneiro, D. Sánchez, J. Fontcuberta, *Phys. Rev. B* **2001**, *64*, 180406.
- [95] W. Westerburg, D. Reisinger, G. Jakob, *Phys. Rev. B* **2000**, *62*, R767.
- [96] D. Sánchez, M. García-Hernández, N. Auth, G. Jakob, *J. Appl. Phys.* **2004**, *96*, 2736.
- [97] T. Fix, D. Stoeffler, S. Colis, C. Ulhaq, G. Versini, J. P. Vola, F. Huber, A. Dinia, *J. Appl. Phys.* **2005**, *98*, 023712.
- [98] M. Besse, F. Pailloux, A. Barthelemy, K. Bouzouhouane, A. Fert, J. Olivier, O. Durand, F. Wycisk, R. Bisaro, J.-P. Contour, *J. Cryst. Growth* **2002**, *241*, 448.
- [99] H. Jalili, N. F. Heinig, K. T. Leung, *J. Chem. Phys.* **2010**, *132*, 204701.
- [100] I. Angervo, M. Saloaro, J. Tikkanen, H. Huhtinen, P. Paturi, *Appl. Surf. Sci.* **2017**, *396*, 754.
- [101] I. N. Stranski, L. Krastanow, *Monatsh. Chem.* **1937**, *71*, 351.
- [102] T. Fix, G. Versini, J. L. Loison, S. Colis, G. Schmerber, G. Pourroy, A. Dinia, *J. Appl. Phys.* **2005**, *97*, 024907.
- [103] D. Kumar, D. Kaur, *Phys. B* **2010**, *405*, 3259
- [104] H. Asano, Y. Kohara, M. Matsui, *Jpn. J. Appl. Phys.* **2002**, *41*, L1081.
- [105] R. Boucher, *J. Phys. Chem. Solids* **2005**, *66*, 1020.
- [106] U. Aschauer, R. Pfenninger, S. M. Selbach, T. Grande, N. A. Spaldin, *Phys. Rev. B* **2013**, *88*, 054111.
- [107] M. Volmer, A. Weber, *Z. Phys. Chem.* **1926**, *119*, 277.
- [108] R. W. Hoffman, *Thin Solid Films* **1976**, *34*, 185.
- [109] M. Saloaro, S. Majumdar, H. Huhtinen, P. Paturi, *J. Phys.: Condens. Matter* **2012**, *24*, 366003.
- [110] M. Saloaro, H. Deniz, H. Huhtinen, H. Palonen, S. Majumdar, P. Paturi, *J. Phys.: Condens. Matter* **2015**, *27*, 386001.
- [111] D. Sanchez, N. Auth, G. Jakob, J. L. Martínez, M. García-Hernández, *J. Magn. Magn. Mater.* **2005**, *294*, e119.
- [112] H. Jalili, N. F. Heinig, K. T. Leung, *J. Appl. Phys.* **2009**, *105*, 034305.
- [113] A. H. Johnson, P. Morris, R. Ricciardo, P. M. Woodward, *Thin Solid Films* **2017**, *622*, 48.
- [114] C. Du, R. Adur, H. Wang, A. J. Hauser, F. Yang, P. C. Hammel, *Phys. Rev. Lett.* **2013**, *110*, 147204.
- [115] A. Di Troilo, R. Larciprete, A. M. Testa, D. Fiorani, P. Imperatori, S. Turchini, N. Zema, *J. Appl. Phys.* **2006**, *100*, 013907.
- [116] A. J. Hauser, R. E. A. Williams, R. A. Ricciardo, A. Genc, M. Dixit, J. M. Lucy, P. M. Woodward, H. L. Fraser, F. Yang, *Phys. Rev. B* **2011**, *83*, 14407.
- [117] A. Venimadhav, F. Sher, J. P. Attfield, M. G. Blamire, *J. Magn. Magn. Mater.* **2004**, *269*, 101.
- [118] H. Deniz, D. Preziosi, M. Alexe, D. Hesse, *J. Appl. Phys.* **2017**, *121*, 023906.
- [119] N. Kumar, P. Misra, R. K. Kotla, A. Gaur, R. Rawat, R. J. Choudhary, R. S. Katiyar, *Mater. Lett.* **2014**, *118*, 200.
- [120] N. Kumar, V. Pandey, A. Gaur, R. K. Kotnala, *J. Appl. Phys.* **2012**, *112*, 073925.
- [121] N. Kumar, G. Khurana, A. Gaur, R. K. Kotnala, *J. Appl. Phys.* **2013**, *114*, 053902.
- [122] M. Hoffmann, V. N. Antonov, L. V. Bekenov, K. Kokko, W. Hergert, A. Ernst, *J. Phys.: Condens. Matter* **2018**, *30*, 305801.
- [123] Y. H. Huang, M. Karppinen, H. Yamauchi, J. B. Goodenough, *Phys. Rev. B* **2006**, *73*, 104408.
- [124] D. Stoeffler, C. Etz, *J. Phys.: Condens. Matter* **2006**, *18*, 11291.
- [125] H. Sakuma, T. Taniyama, Y. Kitamoto, Y. Yamazaki, *J. Appl. Phys.* **2003**, *93*, 2816.
- [126] J. B. Goodenough, R. I. Dass, *Int. J. Inorg. Mater.* **2000**, *2*, 3.

- [127] Y. Sui, X. Zhang, X. Wang, J. Cheng, W. Su, J. Tang, *J. Appl. Phys.* **2007**, *102*, 023903.
- [128] J.-F. Wang, Z. Li, X.-J. Xu, Z.-B. Gu, G.-L. Yuan, S.-T. Zhang, *J. Am. Ceram. Soc.* **2014**, *97*, 1137.
- [129] R. P. Borges, S. Lhostis, M. A. Bari, J. J. Versluijs, J. G. Lunney, J. M. D. Coey, M. Besse, J.-P. Contour, *Thin Solid Films* **2003**, *429*, 5.
- [130] W.-J. Ji, J. Xu, S.-T. Zhang, Y. B. Chen, J. Zhou, Z.-B. Gu, S.-H. Yao, Y.-F. Chen, *Solid State Commun.* **2013**, *163*, 28.
- [131] J. Navarro, C. Frontera, L. Balcells, B. Martínez, J. Fontcuberta *Phys. Rev. B* **2001**, *64*, 092411.
- [132] J. L. Alonso, L. A. Fernández, F. Guinea, F. Lesmes, V. Martín-Mayor, *Phys. Rev B* **2003**, *67*, 214423.
- [133] M. Tovar, M. T. Causa, A. Butera, J. Navarro, B. Martínez, J. Fontcuberta, M. C. G. Passeggi, *Phys. Rev. B* **2002**, *66*, 024409.
- [134] Y. Bugoslavsky, Y. Miyoshi, S. K. Clowes, W. R. Branford, M. Lake, I. Brown, A. D. Caplin, L. F. Cohen, *Phys. Rev. B* **2005**, *71*, 104523.
- [135] M. Bibes, K. Bouzehouane, E. Barthélémy, M. Besse, S. Fusil, M. Bowen, P. Seneor, J. Carrey, V. Cros, A. Vaurès, J.-P. Contour, A. Fert, *Appl. Phys. Lett.* **2003**, *83*, 2629.
- [136] H. Y. Hwang, S. W. Cheong, N. P. Ong, B. Batlogg, *Phys. Rev. Lett.* **1996**, *77*, 2041.
- [137] D. D. Sarma, S. Ray, K. Tanaka, M. Kobayashi, A. Fujimori, P. Sanyal, H. R. Krishnamurthy, C. Dasgupta, *Phys. Rev. Lett.* **2007**, *98*, 157205.
- [138] K. I. Kobayashi, T. Kimura, Y. Tomioka, H. Sawada, K. Terakura, *Phys. Rev. B* **1999**, *59*, 11159.
- [139] D. Niebieskikwiat, F. Prado, A. Caneiro, R. D. Sánchez, *Phys. Rev. B* **2004**, *70*, 132412.
- [140] J. H. Song, J.-H. Park, Y. H. Jeong, *J. Appl. Phys.* **2005**, *97*, 046105.
- [141] M. García-Hernández, J. L. Martínez, M. J. Martínez-Lope, M. T. Casais, J. A. Alonso, *Phys. Rev. Lett.* **2001**, *86*, 2443.
- [142] H. Q. Yin, J.-S. Zhou, J.-P. Zhou, R. Dass, J. T. McDevitt, J. B. Goodenough, *App. Phys. Lett.* **1999**, *75*, 2812.
- [143] D. Sanchez, N. Auth, G. Jakob, J. L. Martínez, M. García-Hernández, *J. Magn. Magn. Mater.* **2005**, *294*, e119.
- [144] M. Metsanoja, S. Majumdar, H. Huhtinen, P. Paturi, *J. Supercond. Novel Magn.* **2012**, *25*, 829.
- [145] T. Manako, M. Izumi, Y. Konishi, K.-I. Kobayashi, M. Kawasaki, Y. Tokura, *Appl. Phys. Lett.* **1999**, *74*, 2215.
- [146] X. M. Feng, G. H. Rao, G. Y. Liu, W. F. Liu, Z. W. Ouyang, J. K. Liang, *J. Phys.: Condens. Matter* **2004**, *16*, 1813.
- [147] E. K. Hemery, G. V. M. Williams, H. J. Trodahl, *Phys. B* **2007**, *390*, 175.
- [148] X. Wang, Y. Sui, J. Cheng, Z. Qian, J. Miao, Z. Liu, R. Zhu, W. Su, J. Tang, C. K. Ong, *J. Phys.: Condens. Matter* **2007**, *19*, 026215.
- [149] V. Pandey, V. Verma, G. L. Bhalla, R. K. Kotnala, *J. Appl. Phys.* **2010**, *108*, 053912.
- [150] V. Pandey, V. Verma, R. P. Aloysius, G. L. Bhalla, R. K. Kotnala, *Solid State Commun.* **2009**, *149*, 869.
- [151] J. L. MacManus-Driscoll, A. Sharma, Y. Bugoslavsky, W. Branford, L. F. Cohen, M. Wei, *Adv. Mater.* **2006**, *18*, 900.
- [152] A. Gaur, G. D. Varma, *Mater. Sci. Eng. B* **2007**, *143*, 64.
- [153] D.-Y. Kim, J. S. Kim, B. H. Park, J.-K. Lee, J. H. Kim, J. H. Lee, J. Chang, H.-J. Kim, I. Kim, Y. D. Park, *Appl. Phys. Lett.* **2004**, *84*, 5037.
- [154] H. Deniz, D. Preziosi, M. Alexe, D. Hesse, C. Eisenschmidt, G. Schmidt, L. Pintilie, *J. Mater. Sci.* **2015**, *50*, 3131.
- [155] X. Wang, X. Zhang, Y. Sui, J. Cheng, Z. Liu, J. Miao, X. Huang, Z. L. Lu, Z. Qian, W. Su, J. Tang, *J. Appl. Phys.* **2006**, *99*, 081113.
- [156] X. Li, Y. Sun, X. Zhu, R. Ang, W. Lu, W. Song, J. Dai, *J. Appl. Phys.* **2008**, *103*, 083711.
- [157] H. Zheng, J. Wang, S. E. Lofland, Z. Ma, L. Mohaddes-Ardabili, T. Zhao, L. Salamanca-Riba, S. R. Shinde, S. B. Ogale, F. Bai, D. Viehland, Y. Jia, D. G. Schlom, M. Wuttig, A. Roytburd, R. Ramesh, *Science* **2004**, *303*, 661.
- [158] C. Deng, Y. Zhang, J. Ma, Y. Lin, C.-W. Nan, *Acta Mater.* **2008**, *56*, 405.
- [159] J. Hoffmann, S. Schnittger, J. Norpoth, S. Raabe, T. Kramer, C. Jooss, *J. Mater. Res.* **2012**, *27*, 1462.
- [160] N. Kumar, R. P. Aloysius, A. Gaur, R. K. Kotnala, *J. Alloys Compd.* **2013**, *559*, 64.
- [161] R. P. Aloysius, M. Dhankhar, R. K. Kotnala, *J. Alloys Compd.* **2013**, *574*, 335.
- [162] S. Gupta, R. Ranjit, C. Mitra, P. Raychaudhuri, R. Pinto, *Appl. Phys. Lett.* **2001**, *78*, 362.
- [163] L. Balcells, A. E. Carrillo, B. Martínez, J. Fontcuberta, *Appl. Phys. Lett.* **1999**, *74*, 4014.
- [164] Z. C. Xia, S. L. Yuan, F. Tu, C. Q. Tang, G. Peng, G. Q. Zhang, L. Liu, J. Liu, Z. Y. Li, Y. P. Yang, C. S. Xiong, Y. H. Xiong, *J. Phys. D: Appl. Phys.* **2002**, *35*, 177.
- [165] A. Gaur, G. D. Varma, H. K. Singh, *J. Phys. D: Appl. Phys.* **2006**, *39*, 3531.
- [166] D. K. Petrov, L. Krusin-Elbaum, J. Z. Sun, C. Feild, P. R. Duncombe, *Appl. Phys. Lett.* **1999**, *75*, 995.
- [167] O. A. Shlyakhtin, K. H. Shin, Y.-J. Oh, *J. Appl. Phys.* **2002**, *91*, 7403.
- [168] C.-H. Yan, Z.-G. Xu, T. Zhu, Z.-M. Wang, F.-X. Cheng, Y.-H. Huang, C.-S. Liao, *J. Appl. Phys.* **2000**, *87*, 5588.
- [169] J. Kumar, R. K. Singh, H. K. Singh, P. K. Siwach, N. D. Kataria, R. Singh, O. N. Srivastava, *J. Magn. Magn. Mater.* **2006**, *299*, 155.
- [170] S. A. Köster, V. Moshnyaga, K. Samwer, O. I. Lebedev, G. van Tendeloo, O. Shapoval, A. Belenchuk, *Appl. Phys. Lett.* **2002**, *81*, 1648.
- [171] M. A. López-Quintela, L. E. Hueso, J. Rivas, F. Rivadulla, *Nanotechnology* **2003**, *14*, 212.
- [172] P. Kameli, H. Salamati, A. Aezamiet, *J. Alloys Compd.* **2008**, *450*, 7.
- [173] J. M. D. Coey, A. E. Berkowitz, L. Balcells, F. F. Putris, F. T. Parker, *Appl. Phys. Lett.* **1998**, *72*, 734.
- [174] M. Venkatesan, C. B. Fitzgerald, U. V. Varadaraju, J. M. D. Coey, *IEEE Trans. Magn.* **2002**, *38*, 2901.
- [175] Y.-H. Huang, H. Yamauchi, M. Karppinen, *Phys. Rev. B* **2006**, *74*, 174418.
- [176] X. H. Li, Y. P. Sun, W. J. Lu, R. Ang, S. B. Zhang, X. B. Zhu, W. H. Song, J. M. Dai, *Solid State Commun.* **2008**, *145*, 98.
- [177] R. Eason, *Pulsed Laser Deposition of Thin Films: Applications-Led Growth of Functional Materials*, Wiley, Hoboken, NJ **2007**.
- [178] *Handbook of Thin Film Technology* (Eds: L. I. Maissel, R. Glang), McGraw-Hill, New York, USA **1970**.
- [179] *Handbook of Deposition Technologies for Films and Coatings* (Ed: R. Bunshah), Noyes, Park Ridge, NJ **1998**.
- [180] *Physical Vapor Deposition of Thin Films* (Ed: J. E. Mahan), Wiley, New York, USA **2000**.
- [181] *Handbook of Thin Film Technology* (Eds: H. Frey, H. R. Khan), Springer, Berlin, Heidelberg, Germany **2015**.
- [182] *Epitaxial Growth of Complex Metal Oxides* (Eds: G. Koster, M. Huijben, G. Rijnders), Elsevier, Cambridge, UK **2015**.
- [183] M. Stafe, A. Marcu, N. N. Puscas, *Pulsed Laser Ablation of Solids: Basics, Theory and Applications*, Springer, Berlin, Heidelberg, Germany **2014**.
- [184] J. Raittila, T. Salminen, T. Suominen, K. Schlesier, P. Paturi, *J. Phys. Chem. Solids* **2006**, *67*, 1712.
- [185] T. Suominen, J. Raittila, P. Paturi, *Thin Solid Films* **2009**, *517*, 5793.
- [186] D. H. A. Blank, M. Dekkers, G. Rijnders, *J. Phys. D: Appl. Phys.* **2014**, *47*, 034006.

- [187] S. Chakraverty, A. Ohtomo, D. Okuyama, M. Saito, M. Okude, R. Kumai, T. Arima, Y. Tokura, S. Tsukimoto, Y. Ikuhara, M. Kawasaki, *Phys. Rev. B* **2011**, *84*, 064436.
- [188] S. Chakraverty, K. Yoshimatsu, Y. Kozuka, H. Kumigashira, M. Oshima, T. Makino, A. Ohtomo, M. Kawasaki, *Phys. Rev. B* **2011**, *84*, 132411.
- [189] S. Chakraverty, X. Z. Yu, M. Kawasaki, Y. Tokura, H. Y. Hwang, *Appl. Phys. Lett.* **2013**, *102*, 222406.
- [190] A. Ohtomo, S. Chakraverty, H. Mashiko, T. Oshima, M. Kawasaki *J. Mater. Res.* **2013**, *28*, 689.
- [191] K. Nishio, H. Y. Hwang, Y. Hikita, *APL Mater.* **2016**, *4*, 036102.
- [192] M. T. Anderson, K. B. Greenwood, G. A. Taylor, K. R. Poeppelmeier, Y. Tokura, *Prog. Solid State Chem.* **1993**, *22*, 197.
- [193] R. H. Hammond, R. Bormann, *Phys. C* **1989**, *162*, 703.
- [194] J. Santiso, A. Figueras, J. Fraxedas, *Surf. Interface Anal.* **2002**, *33*, 676.
- [195] P. Paturi, M. Metsanoja, H. Huhtinen, *Thin Solid Films* **2011**, *519*, 8047.
- [196] S. Kadota, Y. Matsumoto, T. Sasagawa, *Jpn. J. Appl. Phys.* **2011**, *50*, 01BE13.
- [197] M. Santosh, M. Lacotte, A. David, P. Boullay, C. Grygiel, D. Pravartha, G. S. Rohrer, P. A. Salvador, P. Padhan, U. Luders, J. Wang, W. Prellier, *J. Phys. D: Appl. Phys.* **2017**, *50*, 235301.
- [198] J. Santiso, J. Fraxedas, Ll. Balcells, J. Fontcuberta, A. Figueras, *J. Phys. IV* **2001**, *11*, 307.
- [199] S. Wang, H. Pan, X. Zhang, G. Lian, G. Xiong, *Appl. Phys. Lett.* **2006**, *88*, 121912.
- [200] A. H. Johnson, P. Morris, R. Ricciardo, P. M. Woodward, *Thin Solid Films* **2017**, *622*, 48.
- [201] J. A. Thornton. *Annu. Rev. Mater. Sci.* **1977**, *7*, 239.
- [202] Yu-Ran Luo, in *CRC Handbook of Chemistry and Physics*, 91st ed. (Ed: W. M. Haynes), CRC Press, Boca Raton, FL **2010**, Ch. 9.
- [203] C. Du, R. Adur, H. Wang, A. J. Hauser, F. Yang, P. C. Hammel, *Phys. Rev. Lett.* **2013**, *110*, 147204.
- [204] R. Boucher, *J. Magn. Magn. Mater.* **2006**, *301*, 251.
- [205] H. Asano, M. Osugi, Y. Kohara, D. Higashida, M. Matsui, *Jpn. J. Appl. Phys.* **2001**, *40*, 4883.
- [206] N. A. Kalanda, S. E. Demyanov, A. V. Petrov, D. V. Karpinskiy, M. V. Yarmolich, S. K. Oh, S. C. Yu, D.-H. Kim, *J. Electron. Mater.* **2016**, *45*, 3466.
- [207] V. S. Vidyarthi, W.-M. Lin, G. Suchaneck, G. Gerlach, C. Thiele, V. Hoffmann, *Thin Solid Films* **2007**, *515*, 3547.
- [208] X. B. Zhu, J. M. Dai, X. H. Li, B. C. Zhao, S. M. Liu, W. H. Song, Y. P. Sun, *Mater. Lett.* **2005**, *59*, 2366.
- [209] H. Suwaki, T. Yamaguchi, W. Sakamoto, T. Yogo, K. Kikuta, S. Hirano, *J. Magn. Magn. Mater.* **2005**, *295*, 230.
- [210] T. Yamaguchi, H. Suwaki, K. Kikuta, S. Hirano, *Solid State Commun.* **2005**, *133*, 71.
- [211] A. Kazimirov, D. M. Goodner, M. J. Bedzyka, J. Bai, C. R. Hubbard, *Surf. Sci.* **2001**, *492*, L711.
- [212] A. Mami, A. Boukhachem, I. Mellouki, M. Amlouk, *Mater. Lett.* **2019**, *243*, 77.
- [213] J. Rager, A. V. Berenov, L. F. Cohen, W. R. Branford, Y. V. Bugoslavsky, Y. Miyoshi, M. Ardakani, J. L. MacManus-Driscoll, *Appl. Phys. Lett.* **2002**, *81*, 5003.
- [214] Q. Zhang, Z. F. Xu, J. Liang, J. Pei, H. B. Sun, *J. Magn. Magn. Mater.* **2014**, *354*, 231.
- [215] L. V. Kovalev, M. V. Yarmolich, M. L. Petrova, J. Ustarroz, H. A. Terryn, N. A. Kalanda, M. L. Zheludkevich, *ACS Appl. Mater. Interfaces* **2014**, *6*, 19201.
- [216] STREM Chemical Inc., *Metal TMHD Compounds*, [www.strem.com/uploads/resources/documents/metal\\_tmhd\\_compounds.pdf](http://www.strem.com/uploads/resources/documents/metal_tmhd_compounds.pdf) (accessed: August 2019).
- [217] S. Dhar, K. Shalini, S. A. Shivashankar, *Bull. Mater. Sci.* **2008**, *31*, 723.
- [218] J. Musil, D. Heřman, J. Šícha, *J. Vac. Sci. Technol., A* **2006**, *24*, 521.
- [219] G. Suchaneck, R. Labitzke, B. Adolphi, L. Jastrabik, P. Adamek, J. Drahoukoupil, Z. Hubicka, D. A. Kiselev, A. L. Kholkin, G. Gerlach, A. Dejneka, *Surf. Coat. Technol.* **2011**, *205*, S241.